Journal Pre-proof

Thermo-cyclically operated metal oxide gas sensor arrays for analysis of dissolved volatile organic compounds in fermentation processes: Part I – Morphology aspects of the sensing behavior

Binayak Ojha, Margarita Aleksandrova, Matthias Schwotzer, Matthias Franzreb, Heinz Kohler

PII: S2214-1804(23)00010-7

DOI: https://doi.org/10.1016/j.sbsr.2023.100558

Reference: SBSR 100558

To appear in: *Sensing and Bio-Sensing Research*

Received date: 23 January 2023

Revised date: 20 March 2023

Accepted date: 24 March 2023

Please cite this article as: B. Ojha, M. Aleksandrova, M. Schwotzer, et al., Thermo-cyclically operated metal oxide gas sensor arrays for analysis of dissolved volatile organic compounds in fermentation processes: Part I – Morphology aspects of the sensing behavior, *Sensing and Bio-Sensing Research* (2023), https://doi.org/10.1016/j.sbsr.2023.100558

T c compounds in fermentation processes: Part I – Morphology aspects of the sensing behavior

Binayak Ojha[1,*], Margarita Aleksandrova[1], Matthias Schwotzer[2], Matthias Franzreb[2] and Heinz Kohler[1,*]

[1]Institute for Sensor and Information Systems (ISIS), Karlsruhe University of Applied Sciences, Moltkestr. 30, D-76133 Karlsruhe, Germany

[2]Institute of Functional Interfaces (IFG), Karlsruhe Institute of Technology (KIT), Hermann-von-Helmholtz-Platz 1, D-76344 Eggenstein-Leopoldshafen, Karlsruhe, Germany

[*]Corresponding authors.

E-mail addresses: binayak.ojha@h-ka.de (B. Ojha), heinz.kohler@h-ka.de (H. Kohler)

Abstract

For a comparative study of the gas sensing performance to dissolved volatile organic compounds (VOCs), the SnO_2-powders have been prepared using two different fabrication routes; the flame-spray-pyrolysis (FSP) and the sol-gel (SG) route; and were admixed with the same additive-powders (alumina, YSZ, and NASICON). The morphology of the two different SnO_2/additive families were investigated by ESEM analysis and Energy-dispersive X-Ray Spectroscopy (EDS). Both SnO_2/additive material families were separately deposited as thick-film-layers on two four-fold sensor-chips which were simultaneously thermo-cyclically operated in a measurement cell combined with a carrier gas probe, which enables sensing tests with evaporated VOCs (acetic acid, propionic acid, ethanol, acetone) dissolved in water. The resulting Conductance-over-Time-Profiles (CTPs) highlight better sensitivities of most of the FSP-layers to all the analytes compared to the SG-prepared layers. Furthermore, the CTP shapes of the FSP layers show clearly enhanced specificity representing the individual analyte components. This was interpreted to be the consequence of the extremely fine, scarcely agglomerated grain morphology of FSP-prepared powders and their very narrow grain size distribution which provide better conditions for enhanced gas specific surface reactions. Results promise a better chemical analysis capability of dissolved VOCs by numerical analysis of the CTP of FSP-prepared gas sensitive layers.

Keywords: metal oxide, gas sensor, thermo-cyclic operation, flame-spray pyrolysis, VOC analysis

1 Introduction

Chemoresisitive metal oxide gas sensors (MOGs) are well established devices which are discussed for use in many applications like early fire detection in electrical installations [1], flue gas analysis in wood combustion [2], food-quality control [3], public and household security, environmental monitoring, industrial emission control [4] and even in biomedical applications like breath analysis [5,6]. However, this requires clear improvement of the reproducibility of their sensing performance and therefore several steps especially in material science have been done in the last decades to produce well reproducible gas sensing layers with well-defined morphology provided by advanced methods of nanotechnology. Intensive research was focused on the influence of additives in nanoscaled distribution and of the grain size of the matrix material (mostly SnO_2 or ZnO) on the gas sensitivity in general and how sensitivity to specific gas components of interest can be cultivated by those additives. The reader may get a more complete overview from the excellent review of Neri [7], in which several review articles are cited. Meanwhile, several million devices are applied worldwide per year [8] due to their high sensitivity to a large number of oxidizable or reducible gas components [9,10], their rather good long-term stability and simple operation at relatively low costs. However, in spite of this high level of knowledge about the sensing effects, there are still enormous research activities running to gain a deeper understanding of the surface processes at different material morphologies which control the sensor behavior [11]. Simultaneously, there has been continuous evolution of advanced sensor fabrication processes to make this type of sensor also available as microstructure systems integrated in microelectronic devices [12] following the idea to utilize further improved sensor chips for more sophisticated tasks in the field of gas analysis [3]. The latter aspect needs to initiate further research efforts particularly to improve understanding of the influence of the morphology of the gas sensitive metal oxide materials [13], the role of additives on the sensitivity in general, on specific sensitivities desired for special applications and on long-term stability.

Another important aspect concerning utilization of MOGs for analytical purposes is, how to extract as much analytical information as possible from the analyte by use of those devices. MOGs are usually operated at fixed temperature in the range of 300 °C ≤ T ≤ 450 °C. Despite careful selection of additives to attain specific sensitivities, for many applications isothermally operated MOGs lack sufficient discriminating capability to interfering gas components and, as a fact, do not enable gas component identification. Therefore, a single sensor element is considered unsuitable for chemical analysis. In the past, different signal analysis approaches like principle component analysis (PCA) [14,15], artificial neural networks [15–18], multi component analysis (MCA) [19] and pattern recognition methods [19,20] have been developed in order to improve the gas identification capability of isothermally operated MOG-sensor arrays.

mode [21–23], i.e. to vary the operation temperature thermo-cyclically. This operation mode was originally introduced about 25 years ago [24] following the idea that resistance change of the MO-layer is based on gas surface reactions which may be roughly described by the combination of different processes like surface adsorption of the gas molecules, surface chemical reactions with already adsorbed negatively charged oxygen states followed by electron delocalization and desorption of the reaction products. The gas adsorption equilibria and the rates of all these surface processes depend specifically on the reaction process with the individual target molecule and are all specifically and mostly strongly dependent on the temperature. By periodic variation of the sensor temperature the rates of these surface processes are modified periodically. Therefore, thermo-cyclic variation in a triangular shape in time and simultaneous sampling of the conductance results in a molecular specific conductance dependent on temperature but measured over time. The corresponding "conductance fingerprint" represents the specific target molecule interaction with the individual gas sensitive material and adsorbed oxygen species ($O^-_{2\,ads}$, O^-_{ads}, O^{2-}_{ads}) vs. temperature but measured as a conductance–over–time profile (CTP) [25]. However, only if the rate of temperature variation of the sensor is slow enough compared to the kinetics of chemical response (this includes diffusion rates in the porous layer as well as adsorption/desorption and reaction rates), the target gas specific CTP represents a quasi-steady state chemical response. In general, this target gas specific chemical response occurs due to different processes happening at the sensor surface: (1) type of adsorbed oxygen states ($O^-_{2\,ads}$, O^-_{ads}, O^{2-}_{ads}) [26] which varies over the temperature range. (2) oxidation temperature of the analyte, (3) temperature variation rate, (4) layer thickness, grain size and morphology [27]. All these define the diffusion rate and reaction kinetics of gas species in the pores of the layer. In addition, (5) specific reactions at the electrode/metal oxide interfaces [26,28], and (6) specific reactions at the additive/metal oxide interface [21] have to be considered. It was shown that by the numerical analysis of the resulting target gas specific CTPs not only the molecular identification, but even a full analysis by quantitative determination of the gas component concentrations is possible [29]. In addition to enhanced gas analysis capabilities, the periodic variation of the sensor temperature improves sensitivity [30,31] and can reduce long-term drift [32]. All these results confirmed that gas analysis capability of a single sensor can be clearly enhanced by non-isothermal operation, and furthermore the thermo-cyclic operation of an array of different, but well-selected gas sensitive materials is expected to promise even further substantial enhancement of the analytical capability [33].

This work was motivated by the idea to develop a single-chip fourfold array of extremely sensitive MOGs for early analysis of undesired volatile organic acids (VOAs) like acetic acid, propionic acid or butyric acid developing in biogas fermentation processes in presence of different cross sensitive gas components like CO, CH_4 and H_2. This issue needs special pre-treatment of the analyte and the analysis results will be reported in an upcoming paper. Different metal oxides, especially combinations of matrix oxides with different additives like Y doped SnO_2 [34] , Y doped ZnO [35,36] , Pr doped ZnO [37], Co doped $LaFeO_3$ [38], alumina admixed SnO_2 [30], YSZ admixed SnO_2 [30] and NASICON admixed SnO_2[30] were reported for their enhanced acetic

acid s[illegible]s [40], SnO_2 with 3D nanosheets [41] were published to have excellent acetic acid sensing properties. As a general result, it was found, that the sensing properties are clearly influenced by the choice of the additive and by the morphology of the sensitive layers as well.

In this paper, for the first time, the gas sensing characteristics of two simultaneously operated sensor arrays consisting of the same SnO_2/additive layers but differing by differently prepared tin oxide matrix materials were compared. The tin oxide powders were fabricated by (i) the classical sol-gel (SG) route, and (ii) a flame spray pyrolysis (FSP) technique, which leads to different morphologies as disclosed from investigations with an Environmental Scanning Electron Microscope (ESEM). From model gas exposure experiments with VOAs, whose development in biogas fermentation processes is undesired and continuous monitoring, of VOAs is still a loophole in process analysis, the authors expected new insight with respect to the analysis capability of those substances at thermo-cyclic operation of the sensor chips. So called conductance-over-time-profiles (CTPs) of thermocyclically operated every chemoresistive gas sensitive layers were found to depend individually on the gas analyte exposed [25]. Here, new disclosures about (i) the influence of the additive on the individual shape of the CTPs with respect to the target VOC and (ii) the sensitivities of the layers and specificity of the CTP shapes dependent on the layer-morphology, are reported. The latter aspect is of fundamental importance for high quality chemical monitoring of the VOCs by numerical analysis of the CTPs [21].

2 Methodology of the gas analysis concept

The concept of in-situ analysis of dissolved VOCs in water by operation of a carrier gas probe with a thermo-cyclically operated MOG sensor array is illustrated with a sketchy drawing of the experimental setup in [21]. A constant carrier gas stream is lead in stainless steel gas permeation channels covered by a gas permeable membrane (silicone rubber) which separates the carrier gas from the aqueous analyte. Non-dissociatively dissolved VOC permeates through the gas permeable membrane from the liquid phase to the gas phase and is transported with the carrier gas to the measurement cell, complemented with the MOG sensor-array.

Regarding the functional dependency of the analyte concentration in the carrier gas, two aspects must be taken into consideration. First, the partial pressure (p) in the gas phase of physically, i.e., non-dissociatively dissolved VOC for low concentrations is proportional to its concentration (c) in the liquid phase according to Henry's law (eq. 1),

$$p = K_H . c \qquad (1)$$

K_H is the analyte specific Henry's law constant and p is the partial pressure of the analyte in the gas phase in thermodynamic equilibrium with the liquid phase (no gas flow). Indeed, p in the carrier gas is very low. It depends on the gas permeability of the membrane, on the contact time of the carrier gas with the membrane (carrier gas flow rate), and on the temperature.

relative concentration of the analyte in the carrier gas transported to the sensor is the carrier gas flow rate. As lower the flow rate is, as longer is the time for taking up the analyte by the carrier gas permeating across the silicon rubber membrane. Thus, relative concentration of the analyte would reach its maximum at thermodynamic equilibrium, i.e., when the carrier gas flow rate is zero. However, this is impracticable because there would be no gas transported to the sensor chip. Thus, to maximize the sensitivity, a compromise has to be found between high analyte concentration in the carrier gas (low flow rate) to produce high gas sensitivity, and enough analyte transported to the sensor chip, having in mind, that there is some considerable consumption of the analyte at the surface of the MOG by the reaction with (adsorbed) oxygen (Section 1). This aspect was studied in detail (Section 4.1) before the response of different metal oxide layers on various dissolved VOCs was investigated.

The sensor arrays were operated in a sensor cell at the thermo-cyclic mode at temperatures between 150(±5) °C and 450(±5) °C using a triangular heating voltage (Fig. 1a). The sensor measurement cell provides holders for up to two sensor array chips, which can be exposed to analyte gases simultaneously. Generally, the CTPs of all the sensitive layers on sensor arrays together with the resistance of the Pt-meander microstructured on the top side of the chip (Pt-temperature sensor, (Fig.4a) are recorded simultaneously. The Pt-meander resistance is transformed to the actual surface temperature (Fig. 1b) using calibration data experimentally determined in a temperature controlled tubular furnace in advance.

For numerical analysis of the sensor response when exposed to different VOC components (acetic acid, propionic acid, ethanol and acetone), the total absolute changes of the CTPs, i.e., *G-Go* were used, where *Go* is *Go(hum. air) i.e.,* the CTP measured in DI water at pH 7 and *G* is the CTP response measured in presence of the VOC-analyte dissolved in DI water at pH 3. The pH 3 condition makes sure that the VOAs are in the non-dissociated state which is a prerequisite of detection with this method.

The integral value *∑(G-Go)* represents the analyte concentration *c* in the DI water at pH 3 and can be fitted well by a power law (eq.2) [24,42,43] ,which could be used for numerical quantitative chemical analysis in simple cases.

$$\sum(G - Go) = \alpha c^{\beta} \qquad (2)$$

As will be discussed in Section 4.5, the pre-exponential factor α and the power law exponent β are primarily molecular specific constants [44] and are related to the individual surface reaction mechanism at a given temperature [45] as well as on the morphology of the sensing layer [46]. The sensing performance of individual sensing layers for different VOCs is compared in terms of the relative sensor response S. For thermo-cyclically operated MOGs this value had to be defined specifically (eq. 4 in [47]). In this paper this definition had to be applied to the specific issue of investigation (eq. 3). $G_x(VOC)$ is the conductance at a sampling point *x* at dissolved VOC concentration *c* at pH 3, Go_x is the conductance at the same sampling point x measured in presence of DI water at pH 7 and *n* is the total number of sampling points in one measurement cycle; in this case *n*=128.

$S = \frac{1}{n}$ [illegible] GO_x

To get a better overview about the distinctive features of the CTP-shapes, the CTPs were additionally plotted as normalized curves. Normalization was made by the conductance value at the highest temperature (Tmax) of a thermo-cycle. To take this value for normalization may give some impression of arbitrariness. However, it is a peculiar point of conductance at Tmax of thermo-cycle, i.e., at about 450 °C. At this point gas adsorption is mostly unfavorable, i.e., the surface should be mostly clean from adsorbed molecules. On the other hand, reaction kinetics is maximum. Having these behaviors in mind, the resulting normalized CTPs should show the CTP-features generated by surface processes at T<450 °C but related to the (residual) processes at the peak temperature.

3 Experimental

Pure SnO_2 powders of nanoscaled grain size were produced following two different synthesis routes (Section. 3.1), (i) the sol-gel (SG) method and, (ii) the Flame-Spray-Pyrolysis (FSP) method. Each type of powder (SnO_2(SG), SnO_2(FSP)) was admixed with different additive powders, alumina (MZS-1, Martinswerk GmbH), yttrium stabilized zirconia (YSZ) (TZ-8YS, Tosoh Corporation LTD) and NASICON (prepared by our own) by ball milling. Finally, all powders were transferred to printable pastes and deposited on pre-prepared chips (Section. 3.2) with a heater on the reverse side and four inter-digitized electrodes (IDEs) on the top side to fabricate single-chip four-fold sensor-arrays. Thus, four-fold sensor chips of two different kinds were achieved, one with SnO_2(SG)/additive-layers and others with SnO_2(FSP)/additive layers. This means, both kinds of chips provide the same SnO_2/additive-combinations but differ by the kind of SnO_2-powder preparation, by the layer thickness and by limited reproducibility of the layer geometry achieved by micro-dispensing of the pastes.

3.1 Sensitive material synthesis and sensor array fabrication

The sol-gel synthesis route of SnO_2 is described in detail in [30,48]. Pure $SnCl_4$ (Sigma-Aldrich) was slowly dropped in deionized water. The obtained sol was transformed into a gel by addition of ammonia solution. After aging of the gel for 3 weeks it was washed for several times with deionized water and ethanol to get it almost free of the chloride ions. The gel was then stirred, dried and ground for 6 h at 200 rpm in zirconia vessels by ball milling. A fine pale yellow SnO_2 powder was obtained after pre-sintering at 450 °C for 5 h. The XRD diffractograms of those sol-gel prepared SnO_2 powders at 80 °C and 450 °C are shown in Fig. 2.

A very promising alternative route for preparation of extremely fine SnO_2 nanoparticles is the Flame-Spray-Pyrolysis (FSP) method, which is described in detail in [49]. In a recent review [50] the exceptional properties of those FSP prepared nanopowders are illustrated and the different technics of deposition on sensor element substrates by either drop coating and annealing of flame-made nanoparticles or by direct combustion chemical vapor or aerosol deposition are discussed and the

sensin of the liquid precursor (tin(II)-ethylhexanote) in the flame. The size of the nanoparticles is well controlled and depends on the Sn concentration in the precursor and the flame operation conditions. Further, very narrow particle size distributions can be achieved by this novel preparation route. In this work the SnO_2(FSP)-powder was provided by our partner (see acknowledgement). The "drop coating - route" was applied, i.e., the FSP-prepared nanopowders were admixed with additives as introduced above and then transferred to a paste (see Section 3.1.2), which was then deposited on pre-prepared chips with four inter-digitized electrodes (IDEs) by a micro-dispensing technique.

3.1.1 Choice of additive materials and preparation of NASICON

As already mentioned above, two sensor array chips were prepared for comparison of the sensor performance of SnO_2(SG)/additive-layers with SnO_2(FSP)/additive-layers. This means, both chips consist of the same SnO_2/additive-combinations (pure SnO_2, SnO_2/Alumina, SnO_2/YSZ, SnO_2/NASICON) but differ by the SnO_2-preparation routes. Commercial fine powders of alumina and YSZ are available (see above) and were used for preparation of the corresponding pastes for dispensing (see below). However, NASICON ($Na_{1+x}Zr_2Si_xP_{3-x}$, $0 \leq x \leq 3$), one of the most famous sodium solid electrolytes with high sodium ionic conductivity [51] had to be prepared ourselves. The sodium content of the NASICON-framework structure [52,53] can be widely varied and the ionic conductivity achieves its maximum at about x=2 [54]. Due to its rather good chemical stability, NASICON gained rising importance in the last four decades as separator or even as cathode material for high-temperature solid state rechargeable batteries [55,56] and was discussed as a good candidate for development of all solid-state gas sensor elements [57].

NASICON ($Na_3Zr_2Si_2PO_{12}$, x=2) was prepared following a well-known SG-route[58]. $ZrO(NO_3)_2 \cdot 8H_2O$ (Sigma-Aldrich), Na_3PO_4 (Sigma-Aldrich), $Si(C_2H_5O)_4$ (Sigma-Aldrich) and $C_6H_8O_7 \cdot H_2O$ (Carl-Roth GmbH) were individually dissolved in DI water at a specific molar ratio (2:1, 1:1, 2:1, and 2:1), respectively. The silica sol was prepared by continuous admixing of $Si(C_2H_5O)_4$ and DI water at 1:100 volume ratio by continuous magnetic stirring for 2 hours at ambient conditions.

Na_3PO_4, $Si(C_2H_5O)_4$ and $C_6H_8O_7 \cdot H_2O$ solution were added to the silica sol one after the other. The resulting mixture was continuously stirred for 1 h at 50 °C under sealed conditions. The resulting sol was aged for 3 h at 20 °C and was calcinated at 80 °C resulting in a white powder. The powder was ground at 200 rpm for 1 h in zirconia vessels using a planetary ball mill. Afterwards, the powder was sintered at 800 °C for 2 h, at 900 °C for 3 h and at 1000 °C for 4 h successively and all samples were characterized by XRD (Fig. 3). The NASICON-structure was clearly indicated [59]. With increasing sintering temperature the reflections became sharper, i.e. crystallization proceeded, but all XRD diffractograms reveal also some small ZrO_2 impurity phase as also observed in several studies in the past [52,60].

3.1.2

By admixing pure SnO_2 powder with organic binder (DSSP 80 820-MD, Ferro GmbH) and terpineol (Carl-Roth GmbH) by ball milling (planetary ball mill (Fritsch GmbH, Idar-Oberstein, Germany) with two vessels and balls, both made of Zirconia-ceramics) for 2 h at 120 rpm, two different pastes were prepared for micro-dispensing using SG and FSP synthesized SnO_2 as starting powders, respectively. The resulting pastes were denoted as SnO_2(SG) and SnO_2(FSP). For preparation of the SnO_2/additive pastes, the SnO_2(SG) as well as the SnO_2(FSP) powder were first admixed with alumina, YSZ and NASICON(x=2) powders in a volume ratio of 4:1, respectively, by ball milling and then these mixed powders were transferred into pastes by admixing with organic binder and terpineol in the ball mill as just described above. The pastes were denoted as SnO_2(SG), SnO_2(SG)/Alumina, SnO_2(SG)/YSZ, SnO_2(SG)/NASICON, SnO_2(FSP), SnO_2(FSP)/Alumina, SnO_2(FSP)/YSZ, and SnO_2(FSP)/NASICON.

3.2 Fabrication of four-fold MOG sensor array chips

The four-fold MOG sensor array chips (size: 4×4 mm^2) comprise four IDE and a resistive Pt-temperature sensor at the top side and a Pt-heater at the reverse side (Fig. 4). They were prepared using DC sputtering, photolithography and plasma etching techniques [33]. Each Pt-IDE thin film structure consists of ten fingers with 50 µm in width and 50 µm distance to the neighboring fingers. The thin-film Pt-layer thickness is about 1 µm.

On the first sensor array chip (Fig. 4e) four different pastes, namely, SnO_2(SG), SnO_2(SG)/Alumina, SnO_2(SG)/YSZ, and SnO_2(SG)/NASICON were deposited on the Pt-IDEs in thick film form employing a micro-dispensing technique (DOTLINER 06, Martin GmbH, Wessling, Germany). Similarly, on the second chip (Fig. 4d) SnO_2(FSP), SnO_2(FSP)/Alumina, SnO_2(FSP)/YSZ, and SnO_2(FSP)/NASICON were deposited. After dispensing the layers were subsequently dried and then sintered at 700 °C for 20 minutes. The sintered FSP-layers (Fig. 4d) and SG-layers (Fig. 4e) look clearly different. FSP-layers are highly transparent in comparison to SG-layers. There is also clear difference in the layer thickness between FSP-layers and SG-layers (Fig. 7). Additionally, as will be discussed in Sec. 4.2, the ESEM analysis (Fig. 8 and Fig. 10) disclosed that the SG-layers have clearly bigger average particle size and are more densely packed in comparison to the highly porous FSP-layers which have extremely small average particle size. Both aspects are assumed to result in much smaller light scattering intensities of the FSP-layers which in turn may explain the differences in transparency.

Afterwards, both chips were mounted on TO-8 headers using a micro welding technique. Both 4-fold sensor array chips consist of the same SnO_2-additive combinations but differ by the SnO_2 preparation routes (SG and FSP) and this means, differ by the morphology (grain size and distribution) of the SnO_2 as well as by the mean layer thickness and the thickness profile shape (Fig. 4). The surface morphology of the different SnO_2/additive-layers was analyzed using an environmental scanning electron microscope (Quattro, Thermo Fisher Scientific) equipped with a field emission gun (FEG). Some grain compositional analysis

(Figs. rther, the layer thickness of different layers was studied using a confocal microscope (µsurf explorer, NanoFocus AG, Germany).

To investigate the influence of the layer thickness on the sensor response behavior, a third sensor chip with four sensitive SnO_2(SG) - layers of different thickness was prepared (Fig. 4c). Generally, the thickness of the layer is determined by the pressure applied on the paste in the syringe, the viscosity of the paste, the inner diameter of the needle (110 µm) and the velocity of movement across the area to be covered. Layer thickness beyond the thickness of a mono-layer was achieved by repetitive dispensing on previously dispensed and dried layers at ambient conditions before sintering.

3.3 Gas sensing tests

The experimental setup for analysis of physically, this means non-dissociatively dissolved VOCs in the aqueous liquid (18 °C) of a thermostated bioreactor complemented by a carrier gas probe (see also *Methodology of gas analysis*, Section 2) is illustrated in Fig. 5. A carrier gas flow is kept constant by a commercial mass flow controller (MFC), the pH of the analyte is checked by a pH-sensor and homogeneity of the analyte is achieved by continuous stirring. The gaseous analyte as extracted from the liquid sample is led to the measurement cell consisting of two thermo-cyclically operated sensor arrays (SnO_2(SG)/additive-type and SnO_2 (FSP)/additive-type) using a 3-way magnetic valve. This valve allows to expose the sensor arrays alternatively to the sample gas or to dry synthetic air. Continuous cycling of the chip-temperature between 150(±5) °C and 450(±5) °C was achieved by heating the chip with a triangular heating voltage generated from a Keysight 34970A data acquisition unit. Additionally, the same unit measures the 128 conductance sampling points per temperature cycle of each gas sensitive layer of both chips.

3.3.1 Optimization of measurement conditions

As already stated in Section 2, the measurement conditions with respect to the carrier gas flow rate and the temperature cycling period had to be experimentally estimated to optimize the response of such sensor chips. To make this optimization at representative conditions related to the upcoming experiments, two sensor array chips with four sensitive layers each were operated in the measurement cell simultaneously and CTPs of one of the layers, FSP prepared SnO_2(FSP)/1%Pd-layer [49], at exposure to 4% acetic acid dissolved in DI water at pH 3, were analyzed at a cycle-time of 3 min at different carrier gas flows (2.5, 5, 10 and 20 ml/min). In the next step, at constant carrier gas flow the dependency of the CTP on the temperature cycling period was investigated with the same sensitive layer but at cycling periods of 3 min, 15 min and 30 min. In this case, 2000 ppm acetic acid dissolved in DI water was used as the analyte.

3.3.2

The sensor array consisting of layers with different thickness of SnO_2(SG) (5 µm, 9.4 µm, and 18.2 µm) was exposed to different concentrations of acetic acid (500 ppm, 1000 ppm, and 2000 ppm) dissolved in DI water at pH 3 by use of the setup as described in Section 3.3. The measurements were performed at the optimal carrier gas flow rate of 5 ml/min and at the temperature cycling period of 15 min. The influence of the layer thickness on the CTP shape and the dependency of the CTP integrals on layer thickness is discussed in a representative manner in section 4.3 by illustration of the CTPs measured at 2000 ppm of acetic acid dissolved in DI water at pH 3 as an example (Fig. 12).

3.3.3 Studies of the gas sensing properties

Next, two sensor arrays consisting of SnO_2(FSP)/additive and SnO_2(SG)/additive layers respectively (Figs. 4d and 4e) were aged in the same measurement cell as introduced above at a constant flow (5 ml/min) of synthetic air (about 2 ppm humidity) as provided in the gas bottle by the supplier (Linde GmbH) and at the optimal temperature cycling period of 15 min (see Section. 4.1). The aging of MO gas sensitive layers is necessary [61] to adjust the oxygen defect concentration, to stabilize the morphology (post sintering effects) and to desorb gaseous impurities before the measurements are started. After the conductance values of the sensitive layers did not further change significantly in terms of a day (about 120 hours of continuous thermo-cyclic operation), the latest CTP (synth. air) was taken as the Go(dry air)-curve.

Using the fully aged sensor arrays, all the following conductance measurements were performed at the optimal carrier gas flow rate of 5 ml/min and at the temperature cycling period of 15 min. The sensor responses were studied for different liquid phase concentrations of acetic acid, propionic acid, ethanol and acetone dissolved in DI water at 18 °C, which are relevant for later studies of those compounds in biogas fermentation liquids (see upcoming paper (part II)). Liquid phase concentrations as used for the measurements and corresponding gas phase concentrations at 25 °C as calculated using eq. 2 and K_H (Table 1) are given in Table 2. According to the van't Hoff approximation in systems near ambient temperature [62] the values of K_H generally decrease exponentially with decreasing temperature. For example, calculated K_H(18 °C) for acetic acid is lower than K_H(25 °C) by a factor of 0.985. Thus, the real gas phase concentrations adjusted in the experiments are expected to be slightly lower than the values presented in Table 2. At each concentration step 12 CTPs were recorded and the last CTP was used for data illustration.

Table 1. *Henry constants (25 °C) of the VOCs used in the experiments.*

VOC	K_H / atm.kg.mol^{-1}	Reference
Acetic acid	1.852×10^{-4}	[63]
Propionic acid	1.785×10^{-4}	[63]
Ethanol	5.263×10^{-3}	[64]
Acetone	38.46×10^{-3}	[64]

Table 2 *[illegible] d from eq.2 at T=25 °C.*

Acetic acid / ppm		Propionic acid / ppm		Ethanol / ppm		Acetone / ppm	
Liquid phase	**Gas phase**	**Liquid phase**	**Gas phase**	**Liquid phase**	**Gas phase**	**Liquid phase**	**Gas phase**
100	0.3	100	0.24	-	-	-	-
200	0.6	200	0.48	-	-	-	-
500	1.5	500	1.2	15	1.7	2.5	1.6
1000	3	1000	2.4	30	3.4	5	3.2
2000	6	2000	4.8	60	6.8	15	9.5

4 Results and discussions

4.1 Studies to optimize measurement conditions

As already mentioned in Section 2, first the sensing conditions with respect to carrier gas flow and the temperature cycling period had to be optimized before the performance of the analysis system could be investigated. As an example, Fig. 6a shows the CTP profiles of a SnO_2(FSP)/1%Pd-layer operated at a cycling period of 3 minutes at different carrier gas flow rates when 4% acetic acid was dissolved in DI water at pH 3.

The absolute conductance of the CTPs is lowest for 20 ml/min flow with a characteristic peak at ~335 °C (at 1 min). At a flow rate of 10 ml/min the CTP shows clearly higher absolute conductance and a different CTP shape. A shoulder is observed at ~290 °C (0.8 min) and clear peaks at ~410 °C (1.3 min, while temperature rises and at ~360 °C (1.97 min) while temperature decreased. Further reduction of the flow rate to 5 ml/min resulted in a further small increase of the absolute conductance maximum and the shoulder at heating phase is no more visible. Overall, the CTP shape is sharper in structure and the peaks are observed at ~410 °C (1.35 min) and ~ 380 °C (at 1.88 min). Further decrease of the flow rate to 2.5 ml/min resulted in a clearly lower absolute conductance with reduced CTP features. From these results, it was clear that we must choose between 10 ml/min and 5 ml/min flow rate. However, these measurements were made for 4% acetic acid dissolved in DI water which is much higher than practical requirements considering the measurements of dissolved organic acids in fermentation processes. In all the upcoming experiments the carrier gas probe was operated at a flow rate of 5 ml/min to enable elongated contact of the carrier gas with the gas permeable membrane for optimization of the sensitivity.

At 5 ml/min carrier gas flow rate, the influence of the temperature cycling period on the CTP-integral and shape had to be further investigated. In Fig. 6b CTP profiles of SnO_2(FSP)/1%Pd operated at different cycle times while exposed to 2000 ppm acetic acid dissolved in DI water are given vs. the sampling points (n=128) which allows the comparison of the resulting CTP-features on a common time-base. The CTPs show clearly different absolute conductance and CTP features depending on the temperature rate. For 3 min cycling period, the absolute conductance is the lowest with characteristic peak at ~388 °C (t=0.4) and at ~325 °C (t=0.7). With increased cycling period to 15 min and 30 min, an additional shoulder is observed while heating and

the pe 5 min and 30 min, there is no difference in absolute conductance as well as in CTP features while temperature is decreased. However, while temperature is rising, CTP shape is broader, and the profile shoulder is a little bit better visible at the 30 min cycling period compared with the profile at 15 min. But the differences are not substantial, therefore the 15 min cycling period is used for all further measurements.

4.2 Layer thickness and morphology of the sensitive layers

The topographic image and the average thickness profiles of individual sensitive layers sampled with a confocal microscope are illustrated in Fig. 7. The thickness of the layers is not measured homogeneous. Moreover, each layer shows a laterally different thickness profile and, as desired, varies in absolute thickness. Moreover, the SnO_2(FSP)/additive-layers are typically prepared clearly thinner than the SnO_2(SG)/additive-layers. This has to be considered when comparing the CTPs and response behaviors.

Different morphologies by different routes of preparation: For the ESEM and EDS analysis, special sample-layers were coated with 3 nm thick gold layer. The ESEM-images of the surface morphologies of SnO_2(FSP) and of the SnO_2(FSP)/additive-layers are displayed in Fig. 8. The grain size of the SnO_2(FSP)-layer seems to be very homogeneous and the grain diameter is estimated to about 15 nm. Clear influence of the additives on the SnO_2 grain size is not evident. From the ESEM images and the EDS analyses (Fig. 9a-9c) it is obvious, that the additive grains are not homogenously distributed in the SnO_2(FSP) matrix. This was investigated by EDS point analysis at different areas of the samples. By the EDS-spectra the additive-grains could be rather well localized. They exhibit a wide distribution of grain size (up to about 3 µm) and are clearly larger compared to the SnO_2(FSP) grains. This is especially the case for the SnO_2(FSP)/NASICON-layer. The NASICON-grains were confirmed by EDS analysis in Area-1 and Area-2 (Fig. 9c) by strong peaks of Na, Si and Zr. In the SnO_2(FSP)/Alumina-layer the alumina was confirmed in Area-1 and Area-2 (Fig. 9a) by high peaks of aluminum in the EDS analysis spectra. Similarly, in the SnO_2(FSP)/YSZ-layer (Fig. 9b) YSZ was localized in Area-2 and Area-3 as indicated clearly by additional peaks of Zr, Y close to the Au-peak of the EDS spectra. However, the analysis of Area-1 is different. No significant YSZ-signal (Zr and Y peak) was found.

Similarly, in Fig. 10, the morphology of SnO_2(SG) and of different SnO_2(SG)/additive-layers is illustrated. The SnO_2(SG) matrix consists of crystalline grains with a wide distribution of block sizes and homogenously distributed fine grains. At higher magnification (inset) the big SnO_2-blocks show a sub-structure of compactly packed nanosized particles with diameters smaller than 20 nm. This means the size of the sub-grains is in the same range than that of the grains obtained by the FSP-route (Fig. 8). However, on the SG-route the nano-grains seem preferably to crystallize to bigger crystalline blocks. This effect seems to be hindered by the FSP preparation technique. In contrast to the SnO_2(FSP)/additive layers, in SnO_2(SG)/additive-layers there are SnO_2 grain blocks with size comparable to the grain size of the additives (Fig. 11). This is especially the case for the

SnO_2(SG) and Alumina layers (Fig. 11a) shows peaks of Na, Si as well as by Zr peaks observed for Area-1 (darker grain). Other brighter regions such as, Area-2 and Area-3 clearly represent the SnO_2. In case of SnO_2(SG)/Alumina layers (Fig. 11a), average grain size of tin oxide is obviously bigger than alumina as localized in Area-1 (SnO_2-grain) whereas, Area-2 and Area-3 clearly confirm the presence of alumina by strong Al peaks in the EDS spectra. Similarly, YSZ also seems to have smaller average grain size compared to SnO_2(SG) but appears to be more homogenously distributed in SnO_2(SG) matrix compared to other additives which is confirmed by the presence of the Zr, Y - peak in EDS analysis of all three areas analyzed (Fig. 11b). The difference in morphology may change the electronic interaction scenario of the additives with the tin oxide grains and may take different influence on the gas sensing properties [30].

4.3 Influence of the layer thickness on the CTP shape

The CTPs of SnO_2(SG) with average thickness of 5 µm, 9.4 µm and 18.2 µm, respectively (Fig. 7a) at exposure to 2000 ppm acetic acid are visualized in Fig 12a. Despite of the differences in the absolute thickness and conductance change, mainly in the heating phase of the cycle, the specific conductance peaks occurring with temperature are well reproducible (no peak shift) in all the layers, while the relative peak height is different for different layers. This result indicates that the reactions of the target gas with the adsorbed oxygen states (Section 1) are the same in all the layers, but with different rate. As already mentioned in Section 1, a porous thick film tin oxide layer covering the (underlying) Pt-IDE has to be considered as a chemical reactor with different reaction zones from the top to the metal electrode microstructured on the substrate (outer geom. surface, inner pore surface and electrode/metal oxide – interface, see illustration in [33]) which all provide different (catalytical) reaction conditions. Thus, different (electric) contributions to the overall sensing behavior have to be considered, measured as a change of resistance between the IDE-fingers. As the gas diffuses through the tin oxide layer, a fraction of incident gas is consumed by each of the reaction zones and therefore the fraction of the target gas molecules reaching the lowest zone (electrode/metal oxide – interface) depends on the diffusion and reaction conditions (kind of additive, layer porosity and temperature). In other words, depending on the temperature of the sensitive layer, the layer thickness and its morphology, an effective concentration profile of the reactive gas components in the layer may be formed by which the distribution of sensitivity contributions over the layer thickness is given, which determines the overall sensitivity measured. Of course, this is only an idealized model of the real situation. As shown in Fig. 7, the thickness over a layer is not constant and the edge-effects are also not considered in this crude description. In addition, in case of thermo-cyclically operated tin oxide sensors, if the temperature change (typically) is not slow enough to reach steady state reaction situations, non-steady state situations in the different chemical reaction zones must be considered. This means, each reaction zone is exposed to a different target gas concentration at a time and, probably, different adsorbed oxygen surface state concentration resulting in different individual responses of the reaction zone. Despite these rather complicated reaction conditions, the response over layer thickness seems to be roughly linear (Fig. 12c). The normalized

CTPs (on the thinnest layer (5µm).

4.4 Conductance over time profiles for humidified air and four different VOCs dissolved in DI water

As mentioned in Section 3.2, both sensor arrays (Fig. 4d and 4e) were first aged in dry synthetic air before making measurements with dissolved VOCs in DI water. As an example, in Fig. 13 the CTPs measured for dry synthetic air (Go(dry air)) at the end of the aging process are illustrated together with the CTPs measured for DI water at pH 7(Go(hum air)) as sampled with the carrier gas probe in DI water in the experiment with model acetic acid.

As already introduced in Section 3.3, the concentration ranges of the VOCs chosen for investigation of the sensor responses for each analyte had to be individually set due to their specific Henry constants to enable comparable concentrations in the gas phase. The resulting CTPs as recorded for eight different sensitive layers (columns) when exposed to various concentrations of different VOCs (given in ppm by volume in DI water) like acetic acid, propionic acid, ethanol, and acetone (rows) are visualized in Fig. 14. Obviously, the tin oxide morphology, the additives and, of course, the analyte gas species, take clear influence on the CTP-shapes and the concentration of the analyte is well reflected in the CTP-integral as already reported in former investigations [33] and used for quantitative chemical analysis [29,65]. This means, the individual surface reactions of the gas components on different sensitive layers are observed as VOC specific CTP features which are further illustrated in a normalized representation as shown in Fig. 15. Again, each CTP is normalized by the conductance value as recorded at the maximum temperature of the cycle.

The overview in Fig. 14 illustrates a clear trend. The FSP-layers show specific and well pronounced CTP shapes with the individual gas component but dependent on the kind of additive. In comparison, the SG-layers show those individual feature-characteristics as well, but typically less pronounced. This can be, for instance, very well demonstrated, if the CTPs of SnO_2(FSP)/Al_2O_3 are compared with those of SnO_2(SG)/Al_2O_3 for all four analytes investigated. The individuality of the CTPs dependent on the target gas in case of the SnO_2(FSP)/Alumina – layer is clearly illustrated for all four components (Fig. 14). The CTP shapes of acetic and propionic acid are more similar, however, this is not surprising, because these are molecules with the same functional reaction groups. In contradiction, the CTPs of the SnO_2(SG)/Alumina – layer sampled at exposure to propionic acid, ethanol or acetone, i.e., of molecules with different functional reaction groups, are rather similar in shape and not very different from the shape of a CTP of a pure semiconductor vs. temperature, which is expected to be simply exponential. This means, that those profiles do only to some limited extent represent individual surface reactions of the target gas with the adsorbed oxygen states [33] at specific reaction temperatures. In addition, it is a remarkable fact, that nearly all FSP-prepared layers show a clearly higher dependency of G-Go on the target gas concentrations compared with the SG-prepared layers (Fig. 14). An exception are the pure SnO_2-layers where this difference in sensitivity was only observed at propionic acid exposure.

Fig. 15). Obviously, the CTP-profiles are more or less constant with different concentrations of ethanol or acetone, whereas there is a clear decrease of the specific feature observed in the temperature range between about 300 °C and 400 °C with concentration of acetic acid as well as propionic acid. This behavior tells us, that in case of the carboxylic acids the reaction rate with the oxygen states is still increasing with both, temperature, and concentration, even at the highest temperature of a cycle. In case of ethanol and acetone, the reaction with the target gas seems to be more or less completed beyond some temperature below the maximum temperature Tmax=450 °C. This leads to the increase of the gas specific features with target gas concentration. The corresponding features in the same temperature range but in the second half of the CTP (decreasing temperature) are much less pronounced for all layers. This is a well-known fact [33,65] which is explained by differences in actual gas adsorption correlated with the direction of temperature change in accordance with well-established theories of gas adsorption [66–69].

4.5 Individuality of CTP shapes and comparison of sensor response to model gases.

The individuality of the CTP-shapes at exposure to different analytes is even better illustrated if the normalized CTP-curves from Fig. 15 are plotted into a common diagram. This was done in Fig. 16, which gives an overview about the gas specific CTP-features of all the SnO_2 - and SnO_2/additive – layers under investigation. The features of conductance-change by exposure of different target gas components are clearly different in shape, position, and height (integral) and these "spectra" vary considerably with the kind of additive and morphology of the SnO_2-matrix. The height (integral) of the feature related to the individual target gas component is a measure of the relative response to this specific gas component at temperatures below Tmax. The position of the feature in the range of cyclic temperature variation and its shape represents the individual molecular reactions which are responsible for the conductance change [25]. These differences of the CTP-features related to the kind of target gas component and with respect to the individual SnO_2/additive-layer are clearly demonstrated in Fig. 16. Their peculiarity and reproducibility estimate the quality of chemical gas analysis by numerical analyses of these CTPs as e.g. demonstrated in [25,29]. In general, numerical analysis of the CTP of a sole layer already enables gas component analysis. The analysis quality depends mainly on the individuality of the CTP-features and on their reproducibility. Moreover, the use of a sensor array, namely simultaneous operation of different sensitive layers, provides multiple CTPs which further improves the gas identification quality by application of numerical multi-component analysis and pattern recognition methods [29]. The diagrams demonstrate, that the individuality of the CTP shapes measured on the SnO_2(FSP)/additive-layers related to different gas compounds is clearly better compared with the SnO_2(SG)/additive-layers. Correspondingly, enhanced gas analysis capability with the SnO_2(FSP)/additive-layers can be expected.

Although the CTPs represent reaction states at different temperatures, their integral calculated according to eq. 2 (Fig. 14) vs.VOC concentration is well fitted by a power law. As an example, the integrals and regression curves for SnO_2(SG)/Alumina and

SnO_2(FSP)/Alumina – layer to acetic acid. This trend is confirmed as well by comparative measurements of the absolute gas response of several SnO_2/additive-layers to propionic acid (Fig. 17b). As an overview, the α- and β-values of all studied sensitive layers are given in Table 3. Different trends of the β -values for individual model VOC/layer – combinations are observed. One noticeable trend is the higher β -values for FSP-layers compared to corresponding SG-layers for nearly all the investigated VOCs, except the SnO_2(FSP)NASICON-propionic acid combination.

***Table 3**: Estimated α, β values from regression analysis of ∑(G-Go) on exposure to different model VOCs*

Test gas / Sensitive layer	Acetic acid		Propionic acid		Ethanol		Acetone	
	α	β	α	β	α	β	α	β
SnO_2(FSP)	0.75	0.86	2.83	0.85	9.75	0.92	46.32	0.81
SnO_2 (FSP)/Alumina	1.42	0.88	7.26	0.80	44	0.73	239	0.65
SnO_2 (FSP)/YSZ	1.31	0.85	5.73	0.84	19.6	0.86	77.6	0.81
SnO_2 (FSP)/NASICION	1.26	0.86	15	0.57	16.3	0.79	114.8	0.63
SnO_2 (SG)	0.74	0.85	3	0.66	13.47	0.66	68.27	0.52
SnO_2 (SG)/Alumina	0.37	0.83	1.34	0.65	3.33	0.77	21.27	0.58
SnO_2 (SG)/YSZ	0.68	0.82	2.43	0.68	13.75	0.66	84.02	0.70
SnO_2 (SG)/NASICION	0.92	0.73	2.75	0.59	17.12	0.66	100.63	0.48

4.6 Comparison of gas response

The relative sensor response S (eqn. 3) of the different SnO_2/additive-layers to the VOCs dissolved in DI water at pH 3 is illustrated for the individual concentrations of 1000 ppm, 30 ppm and 5 ppm, respectively, in Fig. 18. As a trend, SnO_2(FSP) and SnO_2(FSP)/additive -layers show significantly higher response to all the tested VOCs compared to the corresponding SG-layers. As an exception, the response of SnO_2(SG)/Alumina to acetic acid is higher than the values of the SnO_2(FSP) and all the SnO_2(FSP)/additive-layers. In fact, among SnO_2(SG) and SnO_2(SG)/additive-layers SnO_2(SG)/Alumina shows the highest response to all the investigated VOCs. This phenomenon cannot be explained by the differences in layer thickness. As visualized in Fig. 7, SnO_2(SG)/Alumina was analyzed as the thinnest layer among SG-layers, however, it shows the highest response. This behavior does not follow the trend discussed in Section 4.3 (Fig. 12).

Furthermore, the response of the SnO_2(SG)/NASICON layer to acetic acid is the lowest although its layer thickness is the highest among the other SG-layers. It is even lower than that of the pure SnO_2(SG)-layer. Surprisingly, for FSP-layers this relation is reverse. The SnO_2(FSP)/NASICON – layer is relatively thin (about 5 µm in average (Fig. 7)) but its response to acetic acid is the highest. In addition, the SnO_2(FSP)/NASICON – layer was measured to show the most pronounced CTP-features when exposed to the four different analytes. This property is very important with respect to the eligibility of those layers for gas analytical purposes and is only scored by the SnO_2(SG)/Alumina-layer (Fig. 13).

S[illegible]red to acetic acid, although the functional reaction group of acetic and propionic acid are the same, and they differ only by the molecular chain length. This difference in response is even more enhanced in case of the FSP-layers (Fig. 18). The response of SnO_2(FSP) is enhanced in relation to SnO_2(SG) by a factor of about 20. This substantial increase of the response behavior related to acetic acid was not observed when the layers were exposed to the non-acidic VOCs like ethanol and acetone. Further, in this context SnO_2(FSP)/NASICON seems to be an exception because the corresponding sensitivities to ethanol and acetone were measured to be clearly the highest.

In a first summary and for upcoming discussion, it must be pointed out, that for both acidic analytes considerable changes in gas response are observed when the SnO_2(SG) is admixed with additives. This is not the case for the non-acidic VOCs. In the most cases the sensitivities of the FSP-layers are clearly higher than those of the SG-layers except for the SnO_2(SG)/Alumina-layer. This is highlighted in the large absolute response difference of roughly a factor of 20 of the SnO_2(SG)-layer vs. SnO_2(FSP)-layer and of about a factor of three of the SnO_2(SG)/additive-layers vs. SnO_2(FSP)/additive-layers when they are exposed with propionic acid. In this regard, also the SnO_2(FSP)/NASICON – layer must be discussed as an exception (see Section 4.6). Compared to SnO_2(FSP) and other SnO_2(FSP)/additive composites, SnO_2(FSP)/NASICON showed lowest sensitivity to propionic acid but highest to acetic acid and to other VOCs.

5 Discussion on gas sensing

In a well-accepted model, the gas sensing mechanism of MOGs involves two main steps. First step is the chemisorption of the atmospheric oxygen ($O_{2\ gas}$) by trapping one or two electrons from the conduction band and forming different adsorbed oxygen states ($O^-_{2\ ads}$, O^-_{ads}, O^{2-}_{ads}) as illustrated in eqs. 4-7 [26]. The kind of negatively charged oxygen states depends on the temperature of the adsorbent [26]. The charge is balanced by the formation of an electron depletion layer in the surface near region of the porous metal oxide. The width of this electron depletion layer was defined by the Debye-length [50,70], which mainly depends on the temperature and the density of electron states (NE) of the bulk metal oxide. In this depletion layer the density of the mobile electrons, i.e., the electronic conductance is massively reduced and depends immediately on the density of the charged oxygen surface states.

$$O_{2\ gas} \xrightarrow{T<100\ °C} O_{2\ ads} \quad (4)$$

$$O_{2\ ads} + e^- \xrightarrow{T<150\ °C} O^-_{2\ ads} \quad (5)$$

$$O^-_{2\ ads} + e^- \xrightarrow{200\ °C<T<400\ °C} 2O^-_{ads} \quad (6)$$

$$O^-_{ads} + e^- \xrightarrow{T>400\ °C} O^{2-}_{ads} \quad (7)$$

I[illegible]ade of oxidation reaction with the adsorbed surface oxygen states. Examples of possible reaction mechanisms related to different VOCs are listed in eqs. 8-11 [71–74]. They represent total reactions which may have to be divided into several reaction steps, however, they have in common, that per molecule an individual number of formerly trapped electrons (oxygen surface states) are delocalized by the oxidation reaction. This means, after reaction with the VOC those electrons contribute now to the electron state density in the conduction band of the electron depletion layer (conductance increase) before they are localized again by a following surface oxygen adsorption process (conductance decrease). Overall, these processes when proceeding at environmental air conditions, form a steady state equilibrium situation dominated by the concentration of the target gas component, the temperature, the gas diffusion conditions in the porous layer and the real surface of the adsorbent. The latter is extensively given by the material morphology and porosity, which determine the density of surface reaction sites. This general model of surface reactions with adsorbed oxygen states was already introduced more than three decades ago e.g. by McAleer et al. [75]. The electric conductance variations by such surface chemical processes are characterized by a more or less increase in the conductance of the electron depletion layer of the porous MO-layer in case of reactions with oxidizable target gas molecules. The difference in conductance related to the value without target gas is defined as the gas response (eq. 3).

$$CH_3COOH + 4O^-_{ads} \rightarrow 2CO_2 + 2H_2O + 4e^- \quad (8)$$

$$CH_3CH_2COOH + 7O^-_{ads} \rightarrow 3CO_2 + 3H_2O + 7e^- \quad (9)$$

$$CH_3CH_2OH + 6O^-_{ads} \rightarrow 2CO_2 + 3H_2O + 6e^- \quad (10)$$

$$CH_3COCH_3 + 8O^-_{ads} \rightarrow 3CO_2 + 3H_2O + 8e^- \quad (11)$$

However, the layer-conductance change with surface reactions, which forms the sensor signal as already described above, depends in a characteristic way on the particle size in relation to the width of the electron depletion layer influenced by the decoration of the particles with catalytically active nanoparticles as a second phase which form a composite. These aspects have been already very well introduced by Morrison [76]. If the average grain diameter of the MO is smaller than double the width of the electron depletion layer [26,70,77], the maximum sensitivity of the layer conductance on the surface chemical reactions can be expected. This grain size of maximum sensitivity is in the range of several nanometers [77]. On the other hand, those porous nanomaterials was speculated to be quite unstable under conditions of high operation temperature due to their high surface energy, which promotes post-sintering effects [7].

In this work, all the sensitivity tests have been conducted in gases extracted from the carrier gas probe immersed in aqueous sample, i.e., all gas atmospheres discussed are assumed to be more or less saturated by water at the given temperature condition of 18° C. This means, for interpretation of the sensing behavior of VOCs dissolved in water the understanding of the

role of [illegible] Being chemisorbed on tin oxide surface, hydroxyl species are formed by molecular dissociation of water which acts as an electron donor [78,79]. This causes direct increase of the conductance (eq. 12).

$$H_2O + O^-_{ads} \rightarrow 2OH_{ads} + e^- \qquad (12)$$

At dynamic operation of the chip-temperature (thermo-cyclic operation mode), as already mentioned above, non-steady state reaction conditions must be considered in particular. This means, according to the Langmuir adsorption model the fractional coverage of the reaction sites by adsorbed oxygen states as well as by target gas molecules depends considerably on the temperature of the gas sensitive layer and, of course, on the reaction kinetics depending on the local temperature and affected by diffusion effects. This parameter, which directly relates to the electronic conductance of the surface near region (electron depletion layer) [75], is now a variable of time. At isothermal operation those surface reactions represent a steady state. However, as investigated in [47], in thermo-cyclic mode, even at cycle-periods beyond 15 min, this is never more correct. The fractional coverage of the adsorbed species depends not only on the actual temperature but also on the direction (positive or negative) of temperature change. This is well indicated by the un-symmetry of the CTPs visualized in. Fig. 14 and Fig. 15.

With regard to the CTP shape sampled from water saturated atmosphere (Go(hum air), Fig. 13), it is clearly illustrated, that the features representing the humidity are much more pronounced as peaks of the CTP from FSP-layers related to those of the SG-layers where typically only small deviations from the Go(dry air)-plot (shoulders) are observed. This again may be interpreted as a hint that the very narrow distribution of the grain size of FSP-layers leads to much sharper CTP-features.

Not surprising is the fact, that in the same range where characteristic CTP-features of the VOCs are observed, in most cases some characteristic deviations of the CTP(hum air) from the corresponding curves at dry air (CTP(hum air) - CTP(dry air), observed as shoulders or peaks, are located (Fig. 15). According to eqs. 8-11, by reactions of VOCs with oxygen states in every case additional water is produced as a reaction product. This means, that the fractional coverage of water is increased which should enhance the formation of adsorbed hydroxyl species (eq. 13). However, as further demonstrated in Fig. 14, the very most CTP-features sampled from carboxylic acids are clearly larger than the corresponding Go-values. The opposite is the case for the very most CTPs sampled at ethanol and acetone exposure, although the gas phase concentrations are similar (Table 2). This is a very important difference which will be further discussed in a future paper, where analysis of such carboxylic acids in fermentation liquids in presence of other VOCs is emphasized.

Regarding the surface reaction processes with acetic and propionic acid, different possible reaction routes of carboxylic acids on tin oxide surfaces and reaction intermediates are described in the literature. It is well understood that at lower temperature the carboxylic acids dissociate on the metal oxide surface forming surface carboxylate [80–82], surface acetate and propionate. Surface carboxylate may undergo ketonization reaction [83,84] as reported for MgO [85], Al_2O_3 [84,86], TiO_2 [86],

ZrO_2 [(O -> OH), as could be expected in presence of atmospheres with high water vapor partial pressure, seems to suppress the ketonization reaction [88] and formation of aldehyde - as confirmed by IR spectroscopy [88], was reported to prevail [89,90] and a Mars - Van Krevelen mechanism [90,91] has been postulated. The catalytic oxidation reactions of carboxylic acids at highly humid atmosphere were found to start at around 150 °C, forming aldehydes as intermediate products between 200-300 °C. In case of propionic acid in addition to formaldehyde also acetyldehyde formation was indicated before complete oxidation at round 300-350 °C takes place [89]. Similarly, the formation of ketene and acrolein from the surface acetate and propionate respectively by dehydration reaction was reported for ZnO [82] and TiO_2 [92,93].

Of course, much more surface analytical investigations would be necessary to correlate these specific reactions with the specific profile structures of the CTPs (Fig. 14 and Fig. 15) of the individual layers. However, by analyzing the features (reaction peaks) of the CTPs produced under well-defined atmospheric conditions, the interaction of acetic and propionic acid on thermo-cyclically operated SnO_2/additive layers seems to occur at the temperature range of 320-390 °C and 300-370 °C for acetic and propionic acid, respectively. This indicates similar underlying gas reactions in all the layers under investigation.

Typically, higher absolute G-Go values and pronounced gas specific features on CTPs when exposed to propionic acid compared to acetic acid could be related to (i) different numbers of electrons per molecule transferred to the conduction band by surface reaction with oxygen states (compare eq.9 with 10) and/or (ii) to the higher catalytic activity of tin oxide for propionic acid [47]. The measured overall conductance of a CTP and its profile structure reflects the specific gas reactions. In this context contributions from the grain surface, the grain bulk, the IDE/MO interface and from the grain boundaries have to be considered [33]. The latter one is highly influenced by the grain size and the width of the sintered necks, which form the contacts between the grains [77].

The clearly higher pronounced CTPs features, and higher gas response observed for FSP-layers compared to SG-layers at exposure to carboxylic acids as well as to ethanol and acetone (Fig. 14-16) obviously is associated with its different morphology. Smaller average grain size and higher porosity of FSP-layers (Fig. 8 and Fig. 9) provide larger active surface area for gas reaction, as well as increased contribution of the depletion layer in relation to the bulk to the overall conductivity as already discussed above and in several studies [26]. Furthermore, it is assumed, that agglomerates from densely packed grains as observed in SnO_2(SG) layers (Fig. 10 and Fig. 11) provide smaller gas penetrability to the reaction sites at the interior of such agglomerates and therefore are less accessible for the gas reactions [94] resulting in reduced gas sensing.

In Fig. 15, which presents normalized CTP profiles, such gas specific features for acetic acid and propionic acid seem to be reduced with increasing gas concentration. This is somehow misleading. Since the data are normalized by the G-Go(hum air)-value measured at maximum temperature of a cycle, at this representation the data indicate that the conductance change at the temperature maximum is relatively higher compared to the change at lower temperature.

ethanol undergoes dissociation by dehydration on acidic oxides forming ethene and water whereas on basic oxides forms acetaldehyde and hydrogen as surface intermediates by dehydrogenation process. Tin oxide is an amphoteric metal oxide [99]. This means that both reaction paths are possible, but the formation of acetaldehyde has been observed to be the thermodynamically more stable reaction product in a temperature range of 150-300 °C [95]. Having the clearly better enhanced individuality of the CTP shapes of FSP-layers in mind (Fig. 13), it is concluded that the surface reaction processes with ethanol seem to be more strongly occurring in SnO_2(FSP) and SnO_2(FSP)/additive composites compared to the corresponding sol-gel prepared layers. This means, that also these processes with ethanol are clearly better reflected in specific CTP-features observed at about 350-400 °C (Fig. 14 and Fig. 15). As already stated above, this aspect is of high relevance with respect to the chemical analysis capability enabled by numerical analysis of the CTPs [29].

Similar quality difference of CTPs is observed at acetone exposure. The interaction of acetone with adsorbed oxygen state (O^-) on metal oxides , such as SnO_2 and ZnO are reported in [68–72]. At relatively higher temperature (≥300°C) acetone reacts with adsorbed oxygen states (O^-) forming acetyl group, formaldehyde radical, methyl radical and CO in different reaction steps before forming CO_2. These reactions are represented as gas specific features for SnO_2(FSP) and SnO_2(FSP)/additive composites at ~300-315 °C as a shoulder (Fig. 15), whereas no specific reaction peaks are observed in case of SnO_2(SG) and SnO_2(SG)/additive composites.

Remarkably specific, individually structured CTP features (Fig. 14-16), which are clearly different in shape when exposed to different analytes, were observed for all FSP-layers. By comparison, the SG-layers generally show different CTP-features as well, but less pronounced and lower sensitivity (G-G0 change vs. analyte concentration). The sensitivity enhancement due to smaller grain size of the FSP-layers was expected (see discussion above), but the enhanced specification of the CTP shape structures, which reflect the individual surface molecular reactions, was discovered by those comparative gas sensing experiments for the first time. The clearly better specificity of the normalized CTPs of the FSP-layers to all analytes under investigation in relation to the SG-layers is also illustrated in Fig. 15.

Another aspect is the relative sensitivity of the layers. As illustrated in Fig. 14, in nearly all cases, the FSP-layer shows the higher CTP-maximum related to the corresponding SG-layer for all analytes exposed. As already stated above, this is not surprising, because the extremely fine FSP-powders and correspondingly highly porous FSP-layers show an extremely large MO-surface, and it can be assumed that the conductance change affects more or less the whole grain volume because the grain diameter is in the range of double the Debye length of the electron depletion layer. This interpretation is also supported by the CTPs plotted in Fig. 13, which illustrate the difference of the CTP(hum air) related to the CTP(dry air). These differences of the FSP-layers are observed formidably bigger in relation to those of the SG-layers. In this context, it is a matter of fact, that the

absolu pared generally thinner (Fig. 7).

Coming back to the CTP-shape structures of the FSP-layers, with regard to the desired capability to analyze the formation of carboxylic acids in fermentation processes well discriminated to other gas components by numerical analysis of such CTP-features [29], the differences of the CTP-shapes related to acetic and propionic acid vs. ethanol and acetone are mostly pronounced by the SnO_2(FSP)/NASICON - and the SnO_2(FSP)/Al_2O_3-layer. It seems that the surface reactions of acetic and propionic acid are catalyzed by the presence of NASICON as already described in [30]. Much higher sensitivities of SnO_2/NASICON-layers in relation to pure SnO_2-layers and clearly different CTP-shapes were explained by a model of (i) specific e^-—Na^+ interaction at the SnO_2/NASICON interface which was assumed to amplify the sensing behavior compared to pure tin oxide [30] and (ii) the catalytic properties of NASICON which may enhance the formation of intermediate products and spillover to O^{2-} surface states at the neighboring SnO_2 grains where they are completely oxidized taking additional influence on the surface depletion layer [100].

The enhanced sensitivity properties of the SnO_2(FSP)/Alumina-layer, may be explained by the existence of Lewis acid sites provided by the alumina, which may influence the dehydration and cracking of the organic molecules [101,102] promoting intermediate products. The combination of these catalytic properties of alumina with surface processes involving those intermediate products and O^{2-} surface states at very fine SnO_2(FSP) grains, as discussed above, may result in pronounced CTP features (Fig. 14 and Fig. 15) and also in improved gas response (Fig. 18).

In relation to SnO_2(FSP)/NASICON, the SnO_2(FSP)/YSZ-layer shows clearly lower response to acetic acid, ethanol, and acetone but it is highest for propionic acid. YSZ is known for its oxygen ion conductivity and its catalytic properties for oxidation reactions [103]. This means, similar to the e^-—Na^+ interaction in SnO_2/NASICON composites an e^- – O^{2-} - interaction over the SnO_2/YSZ-grain boundaries may be presumably assumed here, which could lead to a similar amplification of the sensing behavior of individual carboxylic acids as already discussed for the NASICON additive. Indeed, this enhanced sensitivity of the SnO_2(FSP)/YSZ-composite to carboxylic acids was found in [30] as well. However, in this work the relative sensor response amplification vs. the pure SnO_2(FSP)-layer was found to be not significant (Fig. 18). This may be hypothetically explained by the lower O^{2-}-mobility in YSZ and, of course, the effects of e^- - anion (SnO_2/YSZ) interaction in the (SnO_2/YSZ)-layer has to be expected to be clearly different related to e^- - cation interaction in (SnO_2/NASICON)-layers. Nevertheless, the CTP features observed for SnO_2(FSP)/YSZ are somewhat enhanced as well and show some similarities with those of the SnO_2(FSP)/Al_2O_3-layer. This suggests that the decoration of SnO_2(FSP) with YSZ does not induce other additional surface reactions, but the corresponding CTP-features may be shifted due to different catalytic conditions.

Finally, a general overview about the differences in sensitivity is achieved by a closer look to the power-law exponents (β) and pre-exponential factors (α), as defined by eq. 2 and summarized in table 3. As exemplary illustrated in Fig. 17, the enhanced

sensitized by the differences in morphology, as already discussed above. An exception is the SnO_2/NASICON-layer. In case of acetic acid exposure, the pre-factor α is highest of the group of SG-layers and the lowest of the group of FSP-layers. Hence, at propionic acid exposure the α-value fitted for the SnO_2/NASICON-layers is the largest in both groups of preparation (Table 3), however, the exponential values β are the lowest in each group. This is illustrated by the ΣG-Go - plots in Fig. 17b. In relation to the other SnO_2/additive-layers the SnO_2(FSP)/NASICON-layer attracts attention by a sharp increase of response at propionic acid concentrations below 250 ppm and a markedly lower further increase of response at concentrations beyond. This specific response behavior of the SnO_2(FSP)/NASICON-layer may give an additional hint to the special conditions of gas response of this composite as already discussed above.

6 Conclusions and Outlook

The experiments have impressively shown that SnO_2/additive gas sensitive layers with SnO_2-powder prepared by flame spray pyrolysis (FSP) technique provide considerably better sensitivity to all target gases tested compared to those SnO_2/additive-layers with SnO_2-powder prepared by sol-gel technique. This is the case, although a very fine sub-structure of the sol-gel prepared SnO_2-grains is in a similar range of the grain size as prepared by FSP-technique. Surprisingly, there is not only better sensitivity but also more enhanced specificity of the CTP-features of FSP-prepared SnO_2/additive-layers vs. SG-prepared SnO_2/additive-layers observed when the sensors are thermo-cyclically operated. This was interpreted as the result of the different SnO_2 -morphologies consisting of fine grain networks with high porosity, as provided by the FSP-layers in relation to the SG-prepared layers. It is well known that the FSP-layers provide highly active surface areas for gas reactions, which seem to be one of the key factors favoring target gas - metal oxide - interactions which ultimately result in enhanced gas specific CTP-features. This is highlighted in clearly different, very distinctive CTP-features extracted from the layers related to exposures of acetic or propionic acid and, even more important for analysis, in relation to ethanol and acetone. Furthermore, a characteristic influence of the additives (alumina, YSZ, NASICON(x=2)) on the CTP-features could be disclosed, respectively.

More detailed comparison of the CTP-features achieved by the additives under study revealed remarkable differences in CTP-shapes. This may be a result of specific electron – mobile ion interactions across the common SnO_2/additive – interface when the additive is a solid electrolyte like YSZ or NASICON, as already reported in an earlier study. It is supposed that those interactions may take influence on the target gas reactions with the oxygen surface states. The authors are assured, that such enhanced sensitivities to specific gas components and the specificities of the corresponding CTP-features gained by additives, as observed in these studies, could be even more enhanced, if the additive powders could be prepared with grain sizes similar to those of the SnO_2-grains as prepared by the FSP-technique.

acetic and propionic acid, make the SnO_2(FSP)/additive-layers (additives: alumina, YSZ, NASICON) very promising candidates for monitoring of carboxylic acid development in different processes like e.g., biogas fermentation. In a further step, it is of high interest to investigate how the CTPs of the carboxylic acids are influenced by the presence of other simultaneously developed VOCs in such processes. These aspects have been investigated as well and will be reported in an upcoming publication.

CRediT authorship contribution statement

Binayak Ojha: Methodology, Investigation, Formal Analysis, Software, Visualization, Data Curation, Writing-Original Draft, Writing-Review & Editing. **Margarita Aleksandrova:** Investigation, Formal Analysis. **Matthias Schwotzer:** Investigation, Formal Analysis. **Matthias Franzreb:** Writing-Review & Editing. **Heinz Kohler:** Conceptualization, Methodology, Writing-Original Draft, Writing-Review & Editing, Supervision, Project Administration, Funding acquisition

Declaration of Competing Interest

The authors report no declarations of interest.

Acknowledgements

We are deeply grateful to Prof. Dr. Andreas Güntner, Dept. of Mechanical and Process Engineering, ETH Zürich (CH). for providing the FSP-prepared SnO_2 powder. This work is part of the EBIPREP collaboration project (www.ebiprep.eu) financed by the EU International Programme INTERREG V Oberrhein 2017-2020.

7 References

[1] J. Knoblauch, N. Illyaskutty, H. Kohler, Early detection of fires in electrical installations by thermally modulated SnO2/additive-multi sensor arrays, Sensors and Actuators B: Chemical 217 (2015) 36–40.

[2] B. Ojha, N. Illyaskutty, J. Knoblauch, M.R. Balachandran, H. Kohler, High-temperature CO / HC gas sensors to optimize firewood combustion in low-power fireplaces, J. Sens. Sens. Syst. 6 (2017) 237–246.

[3] V. Galstyan, M. Bhandari, V. Sberveglieri, G. Sberveglieri, E. Comini, Metal Oxide Nanostructures in Food Applications: Quality Control and Packaging, Chemosensors 6 (2018) 16.

[4] N. Yamazoe, Toward innovations of gas sensor technology, Sensors and Actuators B: Chemical 108 (2005) 2–14.

[5] A.T. Güntner, S. Abegg, K. Königstein, P.A. Gerber, A. Schmidt-Trucksäss, S.E. Pratsinis, Breath Sensors for Health Monitoring, ACS sensors 4 (2019) 268–280.

[6] P.H. Rogers, K.D. Benkstein, S. Semancik, Machine learning applied to chemical analysis: sensing multiple biomarkers in simulated breath using a temperature-pulsed electronic-nose, Analytical chemistry 84 (2012) 9774–9781.

[7] G. Neri, First Fifty Years of Chemoresistive Gas Sensors, Chemosensors 3 (2015) 1–20.

[8] F. Sarf, Metal Oxide Gas Sensors by Nanostructures, in: S. Bahadar Khan, A. M. Asiri, K. Akhtar (Eds.), Gas Sensors, IntechOpen, 2020.

[9] (2005) 691–699.

[10] B. Sowmya, J. Athira, P.K. Panda, A review on metal-oxide based p-n and n-n heterostructured nano-materials for gas sensing applications, Sensors International 2 (2021) 100085.

[11] J. Walker, P. Karnati, S.A. Akbar, P.A. Morris, Selectivity mechanisms in resistive-type metal oxide heterostructural gas sensors, Sensors and Actuators B: Chemical 355 (2022) 131242.

[12] G. Eranna, B.C. Joshi, D.P. Runthala, R.P. Gupta, Oxide Materials for Development of Integrated Gas Sensors—A Comprehensive Review, Critical Reviews in Solid State and Materials Sciences 29 (2004) 111–188.

[13] Y. Masuda, Recent advances in SnO2 nanostructure based gas sensors, Sensors and Actuators B: Chemical 364 (2022) 131876.

[14] C. Delpha, M. Siadat, M. Lumbreras, Discrimination of a refrigerant gas in a humidity controlled atmosphere by using modelling parameters, Sensors and Actuators B: Chemical 62 (2000) 226–232.

[15] J. Getino, M.C. Horrillo, J. Gutiérrez, L. Arés, J.I. Robla, C. García, I. Sayago, Analysis of VOCs with a tin oxide sensor array, Sensors and Actuators B: Chemical 43 (1997) 200–205.

[16] A.K. Srivastava, Detection of volatile organic compounds (VOCs) using SnO2 gas-sensor array and artificial neural network, Sensors and Actuators B: Chemical 96 (2003) 24–37.

[17] A. Shahid, J.-H. Choi, A.U.H.S. Rana, H.-S. Kim, Least Squares Neural Network-Based Wireless E-Nose System Using an SnO_2 Sensor Array, Sensors (Basel, Switzerland) 18 (2018).

[18] E. Llobet, J. Brezmes, X. Vilanova, J.E. Sueiras, X. Correig, Qualitative and quantitative analysis of volatile organic compounds using transient and steady-state responses of a thick-film tin oxide gas sensor array, Sensors and Actuators B: Chemical 41 (1997) 13–21.

[19] E. Llobet, R. Ionescu, S. Al-Khalifa, J. Brezmes, X. Vilanova, X. Correig, N. Barsan, J.W. Gardner, Multicomponent gas mixture analysis using a single tin oxide sensor and dynamic pattern recognition, IEEE Sensors J. 1 (2001) 207–213.

[20] U. Weimar, K.D. Schierbaum, W. Göpel, J. Kowalkowski, Pattern recognition methods for gas mixture analysis: Application to sensor arrays based upon SnO2, Sensors and Actuators B: Chemical 1 (1990) 93–96.

[21] K. Frank, V. Magapu, V. Schindler, H. Kohler, H.B. Keller, R. Seifert, Chemical Analysis with Tin Oxide Gas Sensors: Choice of Additives, Method of Operation and Analysis of Numerical Signal, Sen Lett 6 (2008) 908–911.

[22] S. Nakata, H. Okunishi, Y. Nakashima, Distinction of gases with a semiconductor sensor under a cyclic temperature modulation with second-harmonic heating, Sensors and Actuators B: Chemical 119 (2006) 556–561.

[23] P.H. Rogers, S. Semancik, Development of optimization procedures for application-specific chemical sensing, Sensors and Actuators B: Chemical 163 (2012) 8–19.

[24] W.M. Sears, K. Colbow, F. Consadori, General characteristics of thermally cycled tin oxide gas sensors, Semicond. Sci. Technol. 4 (1989) 351–359.

[25] H. Kohler, J. Röber, N. Link, I. Bouzid, New applications of tin oxide gas sensors: I. Molecular identification by cyclic variation of the working temperature and numerical analysis of the signals, Sensors and Actuators B: Chemical 61 (1999) 163–169.

[26] N. Barsan, U. Weimar, Conduction Model of Metal Oxide Gas Sensors, Journal of Electroceramics 7 (2001) 143–167.

[27] Journal Pre-proof (2006) 36–50.

[28] J. Knoblauch, K. Murugavel, H. Kohler, U. Guth, Separation of Sensitivity Contributions in Tin Oxide Thick Film Sensors by Transmission Line Model Measurements at Isothermal and Thermally Modulated Operation, in: Proceedings of Eurosensors 2017, Paris, France, 3–6 September 2017, MDPI, Basel Switzerland, p. 476.

[29] R. Seifert, H.B. Keller, K. Frank, H. Kohler, ProSens—An Efficient Mathematical Procedure for Calibration and Evaluation of Tin Oxide Gas Sensor Data, sens lett 9 (2011) 7–10.

[30] A. Hetznecker, H. Kohler, U. Schönauer, U. Guth, Investigation of SnO2/Na+-ionic conductor composites for new gas sensitive layers, Sensors and Actuators B: Chemical 99 (2004) 373–383.

[31] A. Lee, Temperature modulation in semiconductor gas sensing, Sensors and Actuators B: Chemical 60 (1999) 35–42.

[32] M. Roth, R. Hartinger, R. Faul, H.-E. Endres, Drift reduction of organic coated gas-sensors by temperature modulation, Sensors and Actuators B: Chemical 36 (1996) 358–362.

[33] N. Illyaskutty, J. Knoblauch, M. Schwotzer, H. Kohler, Thermally modulated multi sensor arrays of SnO2/additive/electrode combinations for enhanced gas identification, Sensors and Actuators B: Chemical 217 (2015) 2–12.

[34] L. Cheng, S.Y. Ma, T.T. Wang, J. Luo, X.B. Li, W.Q. Li, Y.Z. Mao, D.J. Gz, High sensitive acetic acid gas sensor based on coral-like and Y-doped SnO2 nanoparticles prepared by electrospinning, Materials Letters 137 (2014) 265–268.

[35] X.B. Li, Q.Q. Zhang, S.Y. Ma, G.X. Wan, F.M. Li, X.L. Xu, Microstructure optimization and gas sensing improvement of ZnO spherical structure through yttrium doping, Sensors and Actuators B: Chemical 195 (2014) 526–533.

[36] N.J. Pineau, F. Krumeich, A.T. Güntner, S.E. Pratsinis, Y-doped ZnO films for acetic acid sensing down to ppb at high humidity, Sensors and Actuators B: Chemical 327 (2021) 128843.

[37] C. Wang, S. Ma, A. Sun, R. Qin, F. Yang, X. Li, J. Li, X. Yang, Characterization of electrospun Pr-doped ZnO nanostructure for acetic acid sensor, Sensors and Actuators B: Chemical 195 (2014) 326–333.

[38] L. Ma, S.Y. Ma, Z. Qiang, X.L. Xu, Q. Chen, H.M. Yang, H. Chen, Q. Ge, Q.Z. Zeng, B.Q. Wang, Preparation of Co-doped LaFeO 3 nanofibers with enhanced acetic acid sensing properties, Materials Letters 200 (2017) 47–50.

[39] J. Luo, S.Y. Ma, L. Cheng, H.S. Song, W.Q. Li, Facile fabrication and enhanced acetic acid sensing properties of honeycomb-like porous ZnO, Materials Letters 138 (2015) 100–103.

[40] W.X. Jin, S.Y. Ma, Z.Z. Tie, W.Q. Li, J. Luo, L. Cheng, X.L. Xu, T.T. Wang, X.H. Jiang, Y.Z. Mao, Synthesis of hierarchical SnO2 nanoflowers with enhanced acetic acid gas sensing properties, Applied Surface Science 353 (2015) 71–78.

[41] T.T. Wang, S.Y. Ma, L. Cheng, X.L. Xu, J. Luo, X.H. Jiang, W.Q. Li, W.X. Jin, X.X. Sun, Performance of 3D SnO2 microstructure with porous nanosheets for acetic acid sensing, Materials Letters 142 (2015) 141–144.

[42] J. Klöber, M. Ludwig, H.A. Schneider, Effects of thickness and additives on thin-film SnO2 gas sensors, Sensors and Actuators B: Chemical 3 (1991) 69–74.

[43] H. Windischmann, P. Mark, A Model for the Operation of a Thin-Film SnO x Conductance-Modulation Carbon Monoxide Sensor, J. Electrochem. Soc. 126 (1979) 627–633.

[44] Journal Pre-proof) 566–573.

[45] D.E. Williams, K.F. Pratt, Microstructure effects on the response of gas-sensitive resistors based on semiconducting oxides, Sensors and Actuators B: Chemical 70 (2000) 214–221.

[46] N. Barsan, U. Weimar, Understanding the fundamental principles of metal oxide based gas sensors; the example of CO sensing with SnO 2 sensors in the presence of humidity, J. Phys.: Condens. Matter 15 (2003) R813-R839.

[47] K. Frank, H. Kohler, U. Guth, Influence of the measurement conditions on the sensitivity of SnO2 gas sensors operated thermo-cyclically, Sensors and Actuators B: Chemical 141 (2009) 361–369.

[48] A. Diéguez, A. Romano-Rodríguez, J.R. Morante, J. Kappler, N. Bârsan, W. Göpel, Nanoparticle engineering for gas sensor optimisation: improved sol–gel fabricated nanocrystalline SnO2 thick film gas sensor for NO2 detection by calcination, catalytic metal introduction and grinding treatments, Sensors and Actuators B: Chemical 60 (1999) 125–137.

[49] N.J. Pineau, S.D. Keller, A.T. Güntner, S.E. Pratsinis, Palladium embedded in SnO2 enhances the sensitivity of flame-made chemoresistive gas sensors, Mikrochimica acta 187 (2020) 96.

[50] A.T. Güntner, N.J. Pineau, S.E. Pratsinis, Flame-made chemoresistive gas sensors and devices, Progress in Energy and Combustion Science 90 (2022) 100992.

[51] H.-P. Hong, Crystal structures and crystal chemistry in the system Na1+xZr2SixP3−xO12, Materials Research Bulletin 11 (1976) 173–182.

[52] H. Kohler, H. Schulz, NASICON solid electrolytes part I: The Na+-diffusion path and its relation to the structure, Materials Research Bulletin 20 (1985) 1461–1471.

[53] H. Kohler, H. Schulz, NASICON solid electrolytes Part II - X-ray diffraction experiments on sodium-zirconium-phosphate single crystals at 295K and at 993K, Materials Research Bulletin 21 (1986) 23–31.

[54] K.-D. Kreuer, H. Kohler, J. Maier, SODIUM ION CONDUCTORS WITH NASICON FRAMEWORK STRUCTURE, in: T. Takahashi (Ed.), High Conductivity Solid Ionic Conductors, WORLD SCIENTIFIC, 1989, pp. 242–279.

[55] M. Guin, F. Tietz, O. Guillon, New promising NASICON material as solid electrolyte for sodium-ion batteries: Correlation between composition, crystal structure and ionic conductivity of Na3+xSc2SixP3−xO12, Solid State Ionics 293 (2016) 18–26.

[56] B. Zhang, K. Ma, X. Lv, K. Shi, Y. Wang, Z. Nian, Y. Li, L. Wang, L. Dai, Z. He, Recent advances of NASICON-Na3V2(PO4)3 as cathode for sodium-ion batteries: Synthesis, modifications, and perspectives, Journal of Alloys and Compounds 867 (2021) 159060.

[57] T. MARUYAMA, Y. SAITO, Y. MATSUMOTO, Y. YANO, Potentiometric sensor for sulfur oxides using NASICON as a solid electrolyte☆, Solid State Ionics 17 (1985) 281–286.

[58] Wang, B., Liang, X. S., Liu, F. M., Zhong, T. G., Zhao, C., Lu, G. Y., & Quan, B. F., Synthesis and characterization of NASICON nanoparticles by sol-gel method, Chemical Research in Chinese Universities 25 (2009) 13–16.

[59] Q. Zhang, Q. Zhou, Y. Lu, Y. Shao, Y. Qi, X. Qi, G. Zhong, Y. Yang, L. Chen, Y.-S. Hu, Modification of NASICON Electrolyte and Its Application in Real Na-Ion Cells, Engineering 8 (2022) 170–180.

[60] asicon Ceramic Electrolytes, J American Ceramic Society 66 (1983) 738–742.

[61] N. Barsan, M. Schweizer-Berberich, W. Göpel†, Fundamental and practical aspects in the design of nanoscaled SnO 2 gas sensors: a status report, Fresenius J Anal Chem 365 (1999) 287–304.

[62] F.L. Smith, A.H. Harvey, Avoid common pitfalls when using Henry's law, Chemical engineering progress 103 (2007) 33–39.

[63] I. Khan, P. Brimblecombe, Henry's law constants of low molecular weight (<130) organic acids, Journal of Aerosol Science 23 (1992) 897–900.

[64] J.R. Snider, G.A. Dawson, Tropospheric light alcohols, carbonyls, and acetonitrile: Concentrations in the southwestern United States and Henry's Law data, J. Geophys. Res. 90 (1985) 3797.

[65] A. Jerger, H. Kohler, F. Becker, H.B. Keller, R. Seifert, New applications of tin oxide gas sensors, Sensors and Actuators B: Chemical 81 (2002) 301–307.

[66] F.S. Stone, Chemisorption and Catalysis on Metallic Oxides, Advances in Catalysis 13 (1962) 1–53.

[67] A. Rothschild, Y. Komem, N. Ashkenasy, Quantitative evaluation of chemisorption processes on semiconductors, Journal of Applied Physics 92 (2002) 7090–7097.

[68] S. Gomri, J.-L. Seguin, J. Guerin, K. Aguir, Adsorption–desorption noise in gas sensors: Modelling using Langmuir and Wolkenstein models for adsorption, Sensors and Actuators B: Chemical 114 (2006) 451–459.

[69] A. Šetkus, Heterogeneous reaction rate based description of the response kinetics in metal oxide gas sensors, Sensors and Actuators B: Chemical 87 (2002) 346–357.

[70] C. Xu, J. Tamaki, N. Miura, N. Yamazoe, Grain size effects on gas sensitivity of porous SnO2-based elements, Sensors and Actuators B: Chemical 3 (1991) 147–155.

[71] Y. Kwon, H. Kim, S. Lee, I.-J. Chin, T.-Y. Seong, W. in Lee, C. Lee, Enhanced ethanol sensing properties of TiO2 nanotube sensors, Sensors and Actuators B: Chemical 173 (2012) 441–446.

[72] Z. El khalidi, B. Hartiti, M. Siadat, E. Comini, H.M.M.M. Arachchige, S. Fadili, P. Thevenin, Acetone sensor based on Ni doped ZnO nanostructues: growth and sensing capability, J Mater Sci: Mater Electron 30 (2019) 7681–7690.

[73] V. Khorramshahi, J. Karamdel, R. Yousefi, Acetic acid sensing of Mg-doped ZnO thin films fabricated by the sol–gel method, J Mater Sci: Mater Electron 29 (2018) 14679–14688.

[74] A. Mirzaei, S.G. Leonardi, G. Neri, Detection of hazardous volatile organic compounds (VOCs) by metal oxide nanostructures-based gas sensors: A review, Ceramics International 42 (2016) 15119–15141.

[75] J.F. McAleer, P.T. Moseley, J.O.W. Norris, D.E. Williams, Tin dioxide gas sensors. Part 1.—Aspects of the surface chemistry revealed by electrical conductance variations, J. Chem. Soc., Faraday Trans. 1 83 (1987) 1323.

[76] S. Morrison, Selectivity in semiconductor gas sensors, Sensors and Actuators 12 (1987) 425–440.

[77] N. Yamazoe, New approaches for improving semiconductor gas sensors, Sensors and Actuators B: Chemical 5 (1991) 7–19.

[78] D. Kohl, Surface processes in the detection of reducing gases with SnO2-based devices, Sensors and Actuators 18 (1989) 71–113.

[79] D. Koziej, N. Bârsan, U. Weimar, J. Szuber, K. Shimanoe, N. Yamazoe, Water–oxygen interplay on tin dioxide surface: Implication on gas sensing, Chemical Physics Letters 410 (2005) 321–323.

[80] Journal Pre-proof araday Trans. 87 (1991) 2647–2653.

[81] H. Gong, Y.J. Wang, S.C. Teo, L. Huang, Interaction between thin-film tin oxide gas sensor and five organic vapors, Sensors and Actuators B: Chemical 54 (1999) 232–235.

[82] J.M. Vohs, M.A. Barteau, Reaction pathways and intermediates in the decomposition of acetic and propionic acids on the polar surfaces of zinc oxide, Surface Science 201 (1988) 481–502.

[83] N. Mansir, H. Mohd Sidek, S.H. Teo, N.-A. Mijan, A. Ghassan Alsultan, C.H. Ng, M.R. Shamsuddin, Y.H. Taufiq-Yap, Catalytically active metal oxides studies for the conversion technology of carboxylic acids and bioresource based fatty acids to ketones: A review, Bioresource Technology Reports 17 (2022) 100988.

[84] R. Pestman, R.M. Koster, A. van Duijne, J. Pieterse, V. Ponec, Reactions of Carboxylic Acids on Oxides: 2. Biomolecular Reaction of Aliphatic Acids to Ketones, Journal of Catalysis 168 (1997) 265–272.

[85] G. MEKHEMER, S. HALAWY, M. MOHAMED, M. ZAKI, Ketonization of acetic acid vapour over polycrystalline magnesia: in situ Fourier transform infrared spectroscopy and kinetic studies, Journal of Catalysis 230 (2005) 109–122.

[86] S.T. Almutairi, E.F. Kozhevnikova, I.V. Kozhevnikov, Ketonisation of acetic acid on metal oxides: Catalyst activity, stability and mechanistic insights, Applied Catalysis A: General 565 (2018) 135–145.

[87] K. Parida, H.K. Mishra, Catalytic ketonisation of acetic acid over modified zirconia, Journal of Molecular Catalysis A: Chemical 139 (1999) 73–80.

[88] Z.-F. Pei, V. Ponec, On the intermediates of the acetic acid reactions on oxides: an IR study, Applied Surface Science 103 (1996) 171–182.

[89] J. Tamaki, T. HAYASHI, Y. YAMAMOTO, M. MATSUOKA, Detection of Aliphatic Carboxylic Acids Using Tin Oxide Based Gas Sensors, Electrochemistry 71 (2003) 468–474.

[90] E.J. Grootendorst, R. Pestman, R.M. Koster, V. Ponec, Selective Reduction of Acetic Acid to Acetaldehyde on Iron Oxides, Journal of Catalysis 148 (1994) 261–269.

[91] R. Pestman, R.M. Koster, J. Pieterse, V. Ponec, Reactions of Carboxylic Acids on Oxides: 1. Selective Hydrogenation of Acetic Acid to Acetaldehyde, Journal of Catalysis 168 (1997) 255–264.

[92] H. Onishi, Y. Yamaguchi, K. Fukui, Y. Iwasawa, Temperature-Jump STM Observation of Reaction Intermediate on Metal−Oxide Surfaces, J. Phys. Chem. 100 (1996) 9582–9584.

[93] K.S. Kim, M.A. Barteau, Pathways for carboxylic acid decomposition on titania, Langmuir 4 (1988) 945–953.

[94] G. Korotcenkov, The role of morphology and crystallographic structure of metal oxides in response of conductometric-type gas sensors, Materials Science and Engineering: R: Reports 61 (2008) 1–39.

[95] T. Jinkawa, G. Sakai, J. Tamaki, N. Miura, N. Yamazoe, Relationship between ethanol gas sensitivity and surface catalytic property of tin oxide sensors modified with acidic or basic oxides, Journal of Molecular Catalysis A: Chemical 155 (2000) 193–200.

[96] E.M. Cordi, J.L. Falconer, Oxidation of Volatile Organic Compounds on Al2O3, Pd/Al2O3, and PdO/Al2O3Catalysts, Journal of Catalysis 162 (1996) 104–117.

[97] C.O. Park, S.A. Akbar, Ceramics for chemical sensing, J Mater Sci 38 (2003) 4611–4637.

[98] Journal Pre-proof uators B: Chemical 9 (1992) 63–69.

[99] L. Shao-you, C. Yuan-dao, Z. Cheng-gang, O. Li-hui, Z. Wei-guo, F. Qing-ge, Solid-Phase Synthesis and Photocatalytic Property of Sulfur and Nickel Doped Tin Oxide Powder Materials by Isomeric Surfactant as Template, J Inorg Organomet Polym 30 (2020) 457–468.

[100] A. Hetznecker, H. Kohler, U. Guth, Enhanced studies on the mechanism of gas selectivity and electronic interactions of SnO2/Na+-ionic conductors, Sensors and Actuators B: Chemical 120 (2007) 378–385.

[101] M. Saha, A. Banerjee, A.K. Halder, J. Mondal, A. Sen, H.S. Maiti, Effect of alumina addition on methane sensitivity of tin dioxide thick films, Sensors and Actuators B: Chemical 79 (2001) 192–195.

[102] T.K. Phung, A.A. Casazza, B. Aliakbarian, E. Finocchio, P. Perego, G. Busca, Catalytic conversion of ethyl acetate and acetic acid on alumina as models of vegetable oils conversion to biofuels, Chemical Engineering Journal 215-216 (2013) 838–848.

[103] M.N. Tsampas, F.M. Sapountzi, P. Vernoux, Applications of yttria stabilized zirconia (YSZ) in catalysis, Catal. Sci. Technol. 5 (2015) 4884–4900.

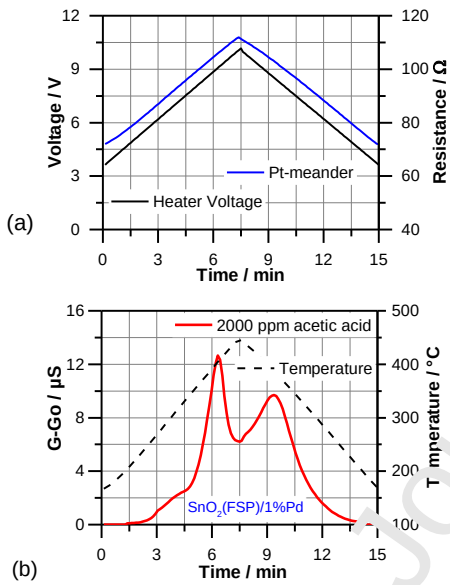

Fig. 1. *Sensor operation methodology. (a) Applied heater voltage over one temperature cycle (black) and corresponding temperature sensor resistance (blue). (b) Temperature vs. time (after calibration of the Pt-meander) and simultaneously measured CTP of one of the layers (SnO_2(FSP)/1%Pd) at acetic acid exposure (red).*

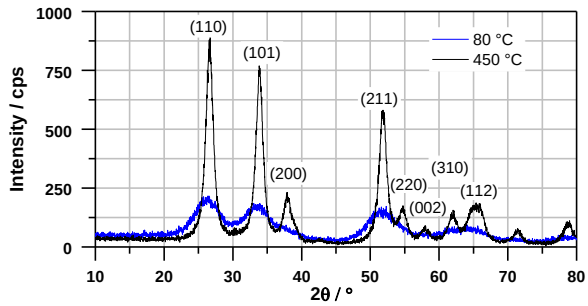

Fig. 2*. XRD diffractograms (Rigaku Miniflex 600, Cu K-alpha) of SnO_2 powder prepared by a sol-gel route and calcinated at different temperatures (80 °C and 450 °C). The diffraction peaks are indicated in accordance with the rutile structure of SnO_2 [33].*

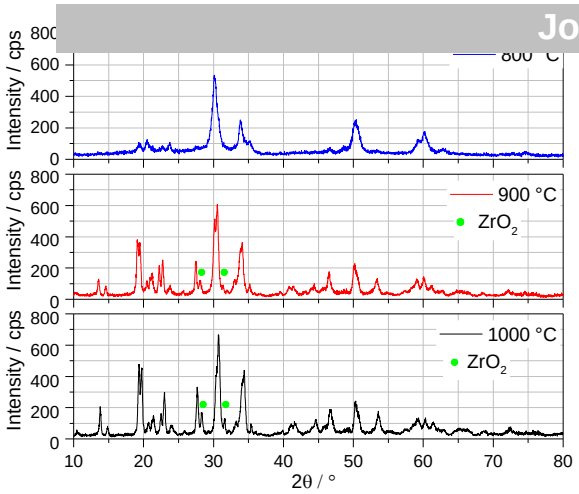

Fig. 3. *XRD diffractograms of NASICON (x=2) powder sintered at different temperatures (800 °C, 900 °C and 1000 °C). The small reflections marked by green dots indicate a small amount of Zirconia as a second phase.*

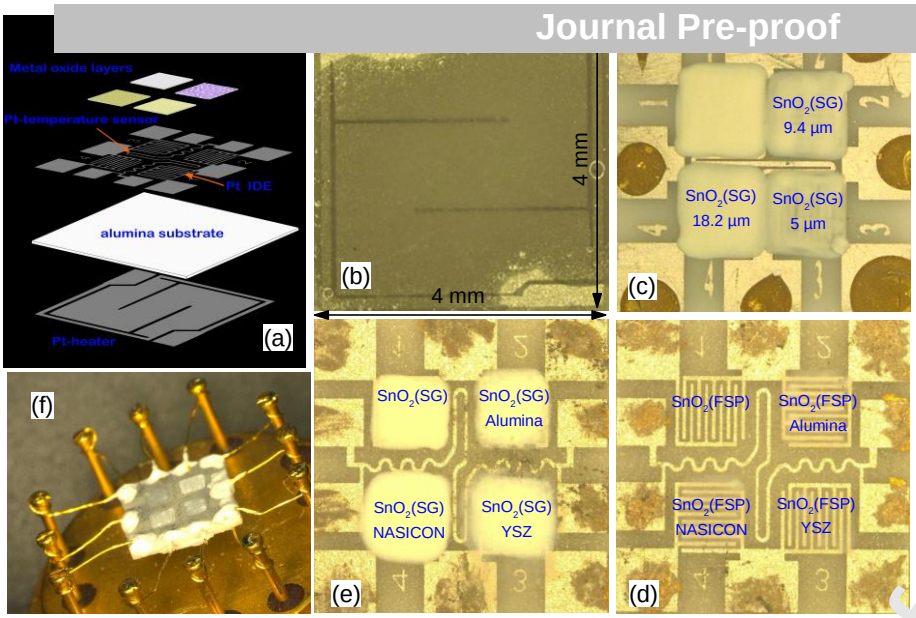

Fig. 4. *Sensor chip preparation and housing. (a) Schematic illustration of different components of a 4-fold sensor chip in exploded view. (b) Glass passivated Pt-heater structure with contact pads on the reverse side of the sensor chip. (c) Sensor array with four different SnO_2(SG) layers with different thickness. (d) Sensor chip deposited with SnO_2(FSP)/additive layers. (e) Sensor chip with IDEs covered by SnO_2(SG)/additive layers. (f) 4-fold sensor array chip mounted on a TO-8 header.*

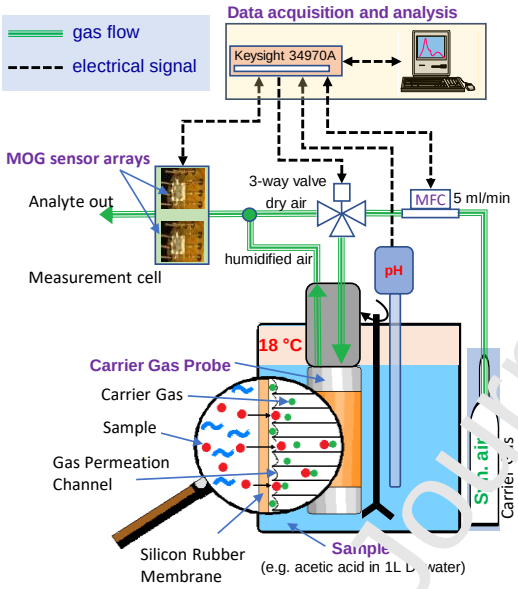

Fig. 5*. Schematic representation of the setup for analysis of dissolved VOC by a combination of a carrier gas probe with two MOG sensor array-chips.*

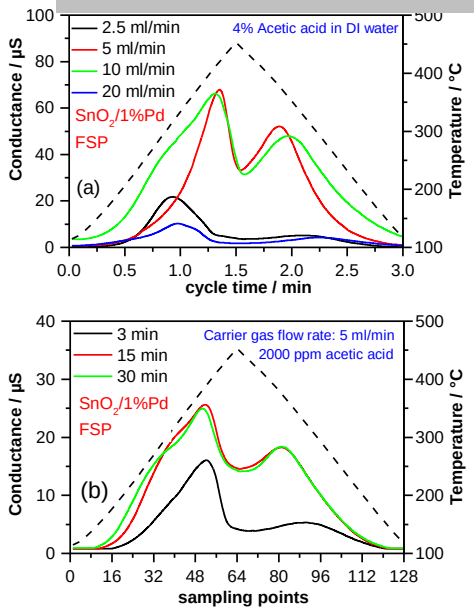

Fig. 6. *CTPs of SnO_2(FSP)/1%Pd when exposed to (a) 4% acetic acid at different carrier gas flow rate and (b) 2000 ppm acetic acid at different cycle time.*

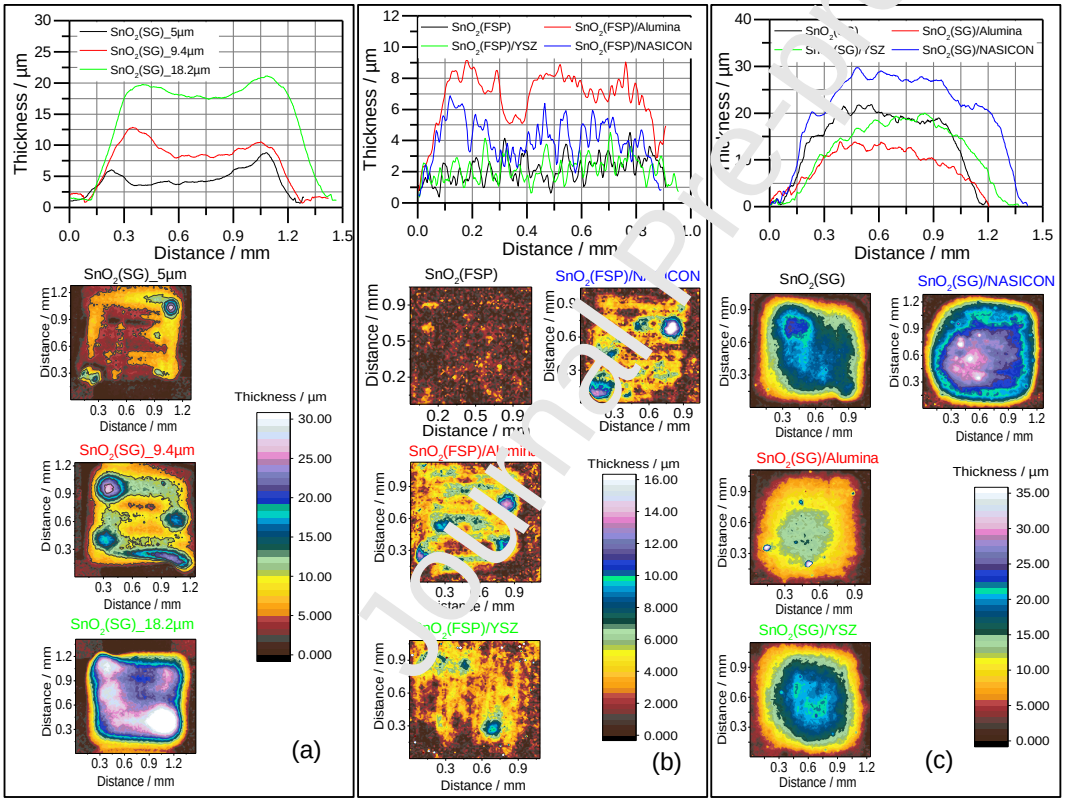

Fig. 7. *Topographic images and line thickness profiles of (a) SnO_2(SG) layers with different thickness (b) SnO_2(FSP)/additive layers and (c) SnO_2(SG)/additive layers*

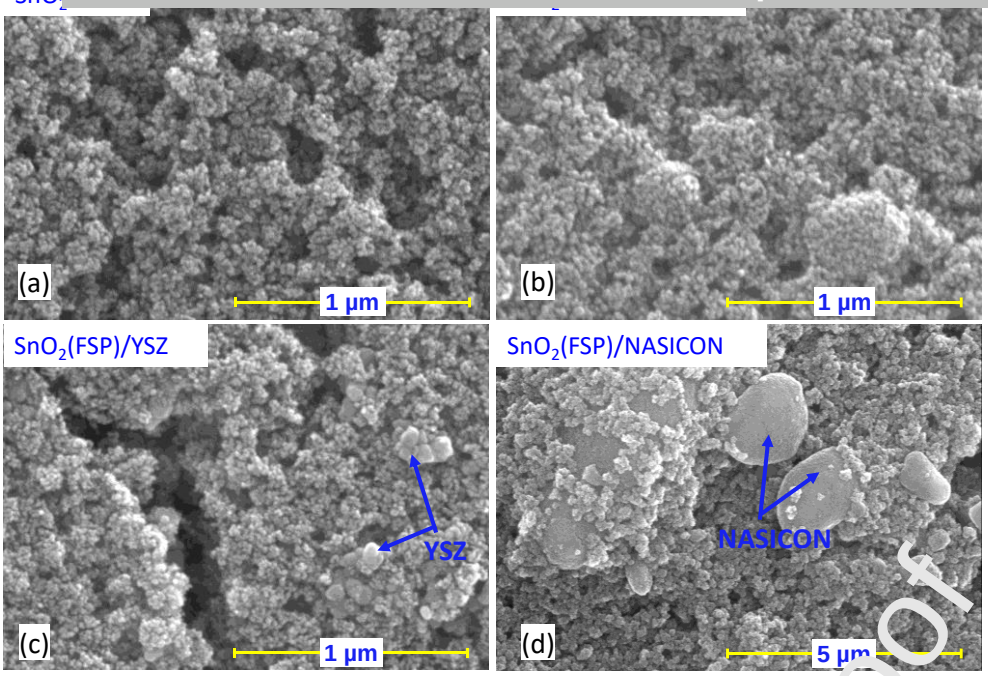

Fig. 8. *ESEM images of different SnO_2(FSP)/additive gas sensitive layers. (a) SnO_2(FSP) (b) SnO_2(FSP)/Alumina (c) SnO_2(FSP)/YSZ and (d) SnO_2(FSP)/NASICON*

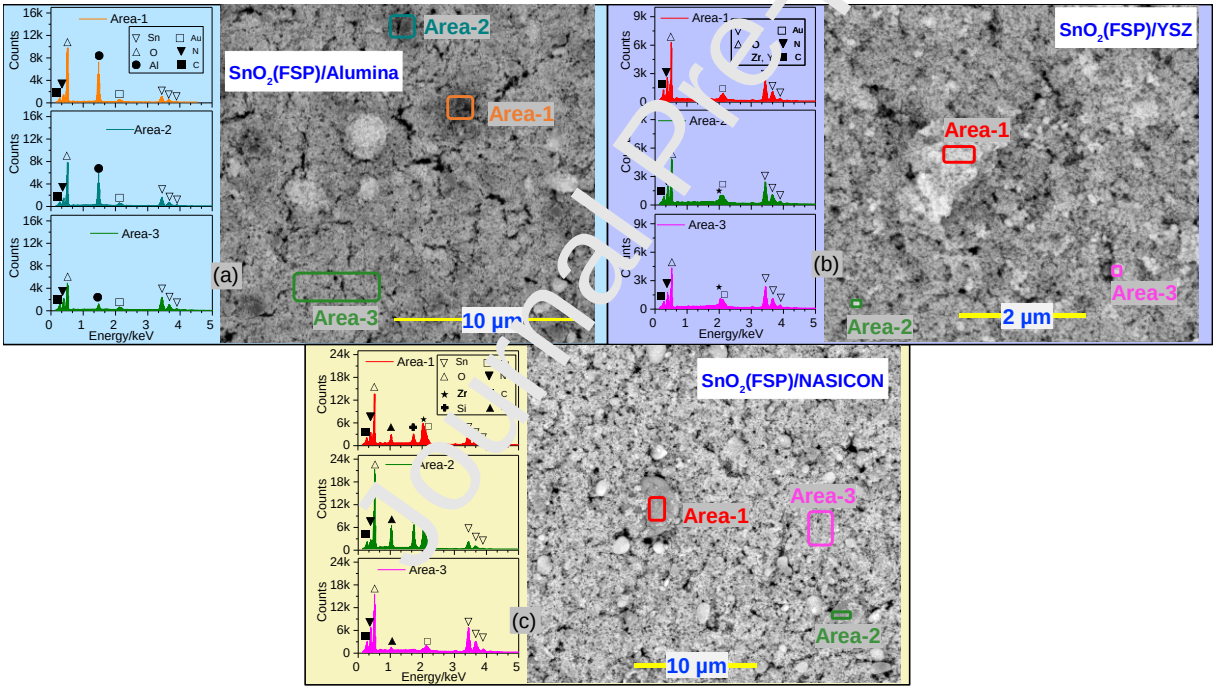

Fig. 9. *ESEM images recorded using backward scattered electron analysis and corresponding spectra of EDS point analysis taken at different areas as indicated in the photographs, respectively. (a) SnO_2(FSP)/Alumina (b) SnO_2(FSP)/YSZ and (c) SnO_2(FSP)/NASICON*

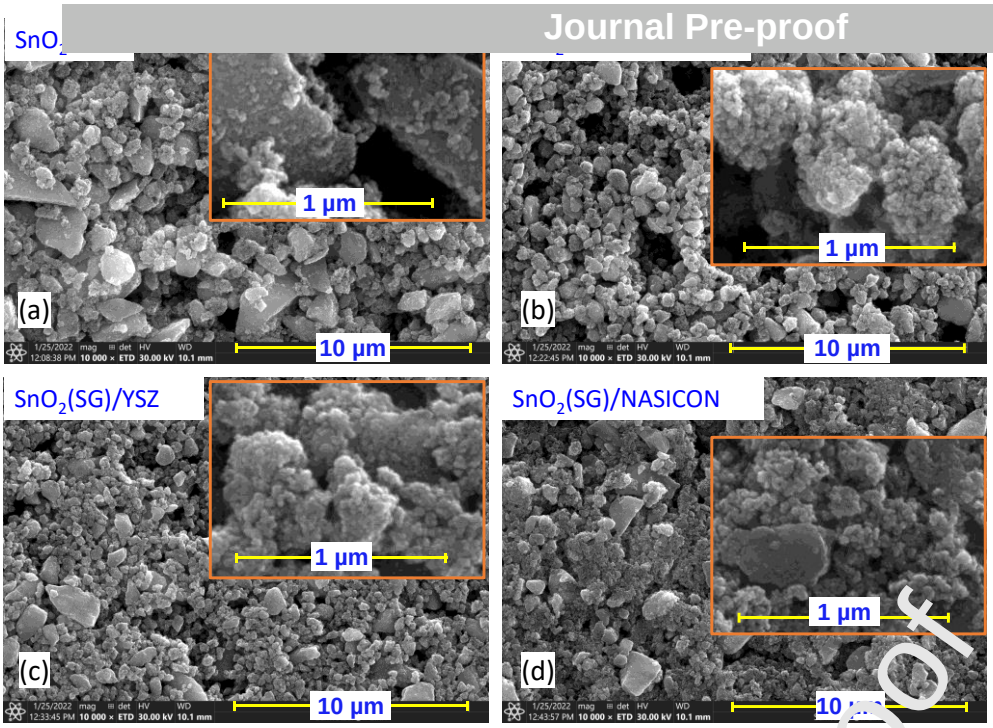

Fig. 10. *ESEM images of different SnO_2(SG)/additive gas sensitive layers. (a) SnO_2(SG) (b) SnO_2(SG)/Alumina (c) SnO_2(SG)/YSZ and (d) SnO_2(SG)/NASICON*

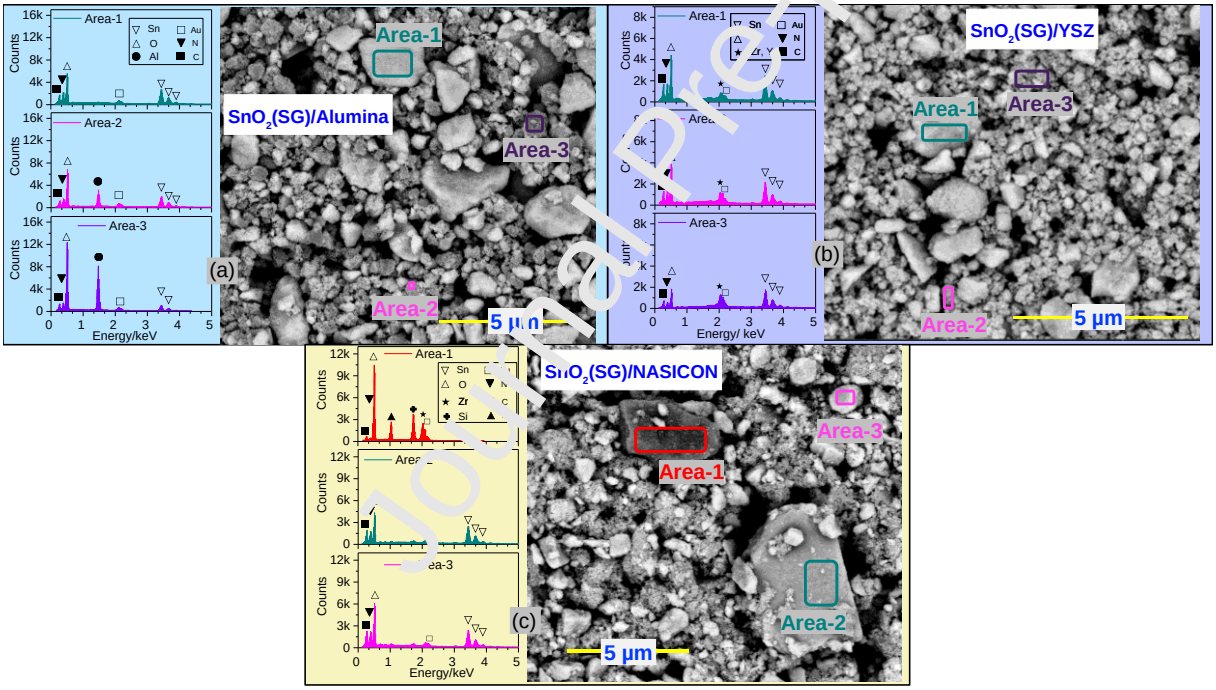

Fig. 11. *ESEM images recorded using backward scattered electron analysis technique and corresponding spectra of EDS point analysis taken at different areas as indicated in the photographs, respectively. (a) SnO_2(SG)/Alumina (b) SnO_2(SG)/YSZ and (c) SnO_2(SG)/NASICON*

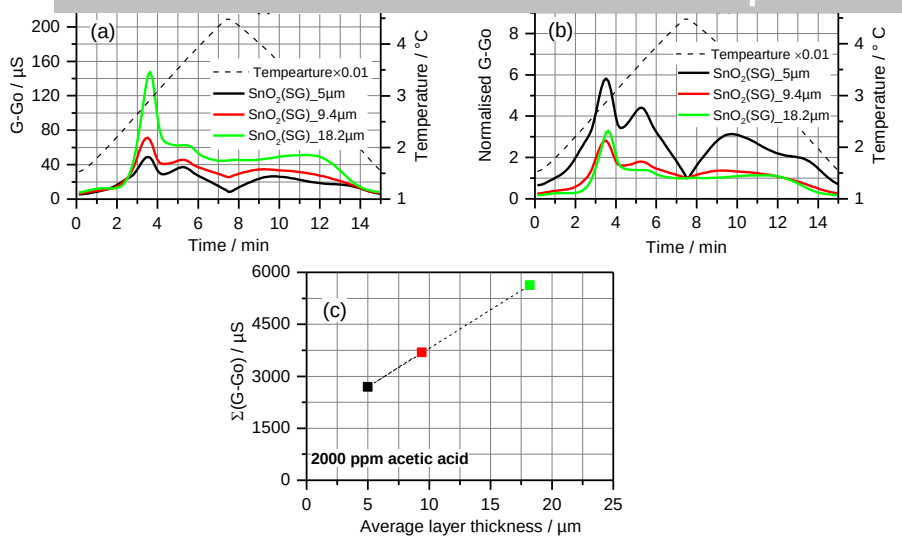

Fig. 12. *Response of SnO_2(SG) layers with different thickness (5 µm, 9.4 µm, and 18.2 µm) on exposure to 2000 ppm acetic acid dissolved in DI water at pH 3. (a) Absolute CTPs, (b) Normalized response and (c) Absolute CTP-integrals vs. layer thickness.*

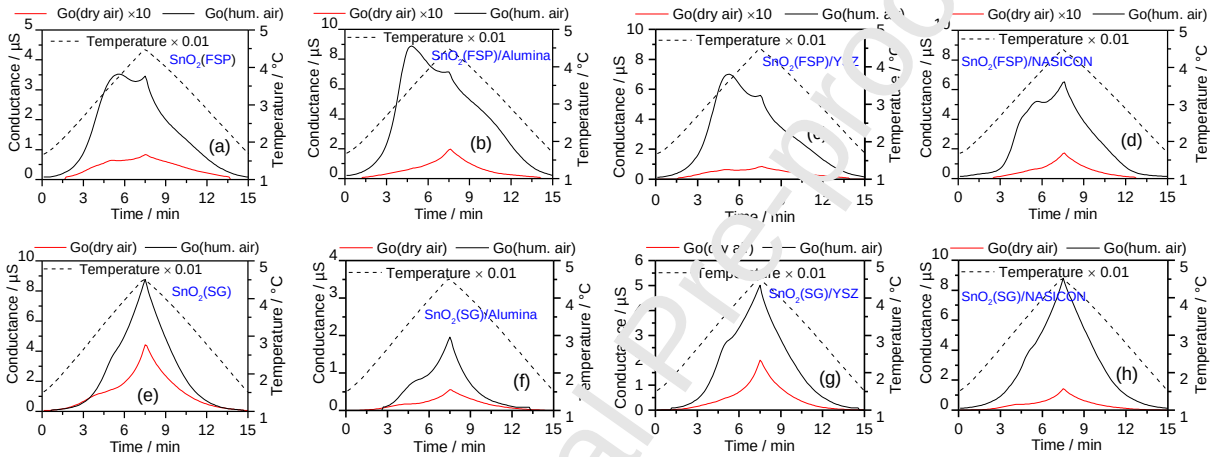

Fig. 13*. Conductance over time profiles (CTPs) of eight different sensitive layers measured for dry synthetic air (Go(dry air) and for humidified air (Go(hum air)) as extracted by the carrier gas probe in DI water at pH 7 prior to the exposure to model VOCs.*

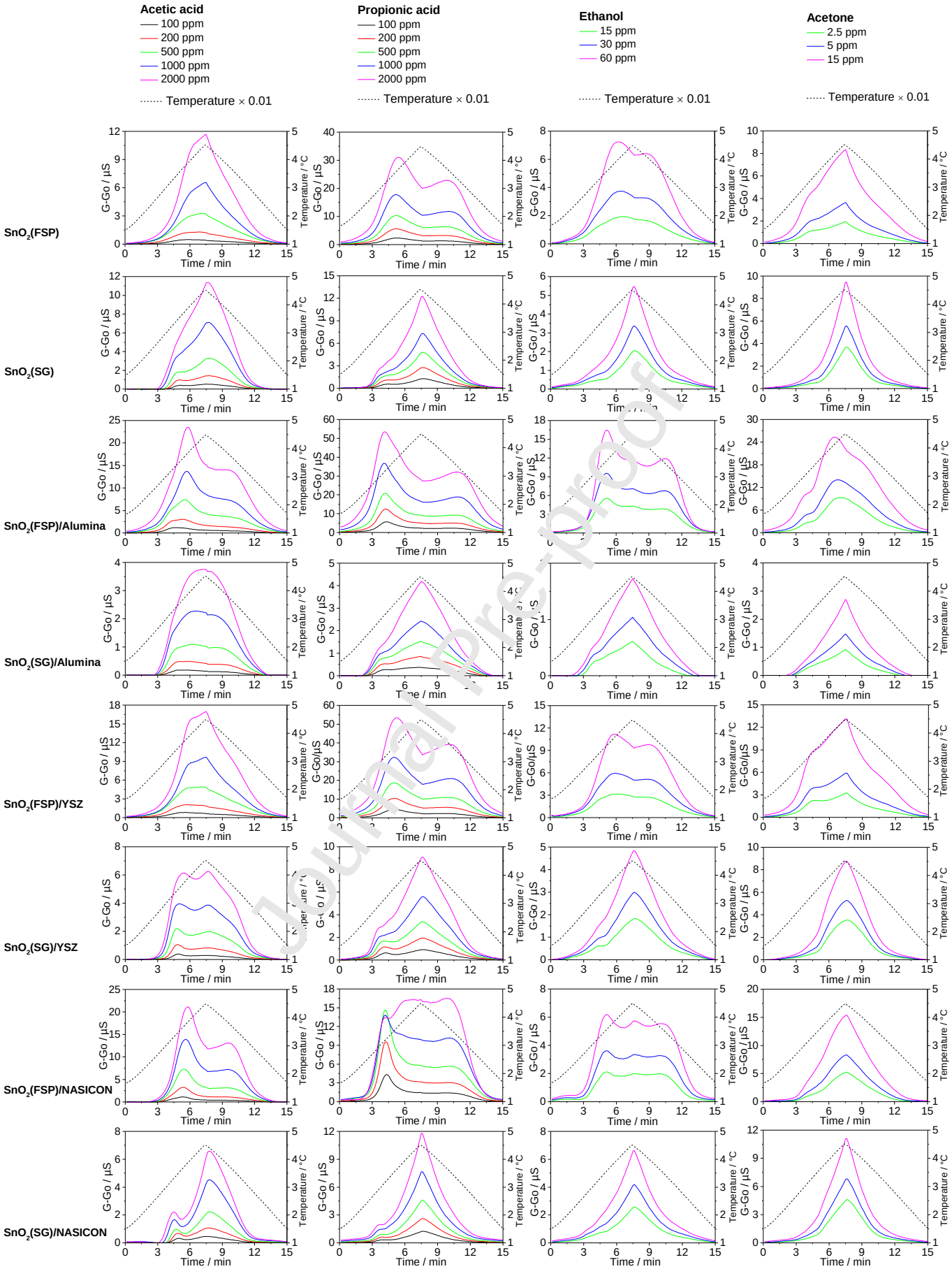

Fig. 14. *Complete sensor responses in the matrix form: Conductance over time profiles (CTP) of eight different sensitive layers (in columns) measured for various concentration of different VOCs (in rows).*

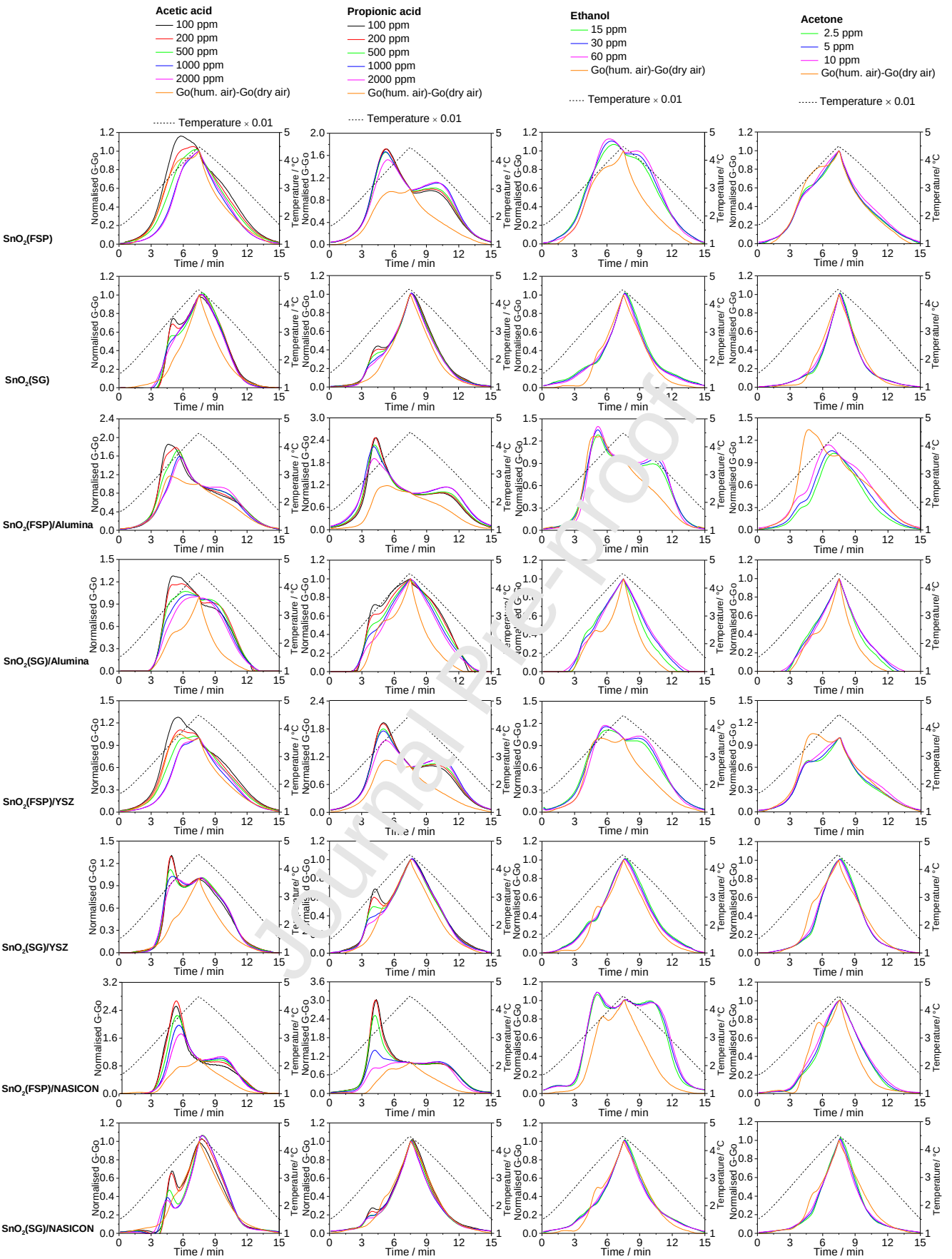

Fig. 15. *Normalized G-Go plots in the matrix form: Conductance over time profiles (CTP) of eight different sensitive layers (in rows) measured for various concentration of different VOCs (in columns). In addition, for every layer the influence of humidity on the base line (Go(dry air)) is illustrated as well as Go(hum air)-Go (dry air) normalized plot. The humidity is related to gas saturation at a water temperature of 18 °C.*

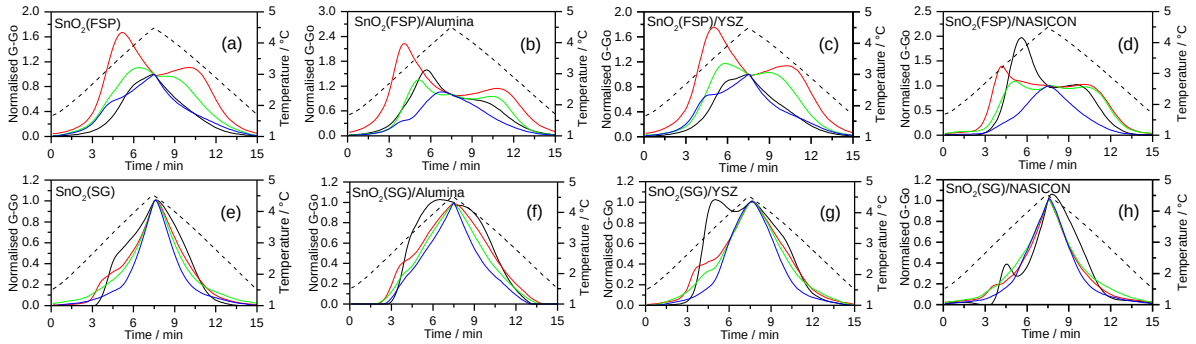

Fig. 16. *Gas specific CTP features of (a) SnO_2(FSP), (b) SnO_2(FSP)/Alumina, (c) SnO_2(FSP)/YSZ, (d) SnO_2(FSP)/NASICON, (e) SnO_2(SG), (f) SnO_2(SG)/Alumina, (g) SnO_2(SG)/YSZ, (h) SnO_2(SG)/NASICON on exposure to 1000 ppm acetic acid, 1000 ppm propionic acid, 30 ppm ethanol, and 5 ppm acetone dissolved in DI water at pH 3.*

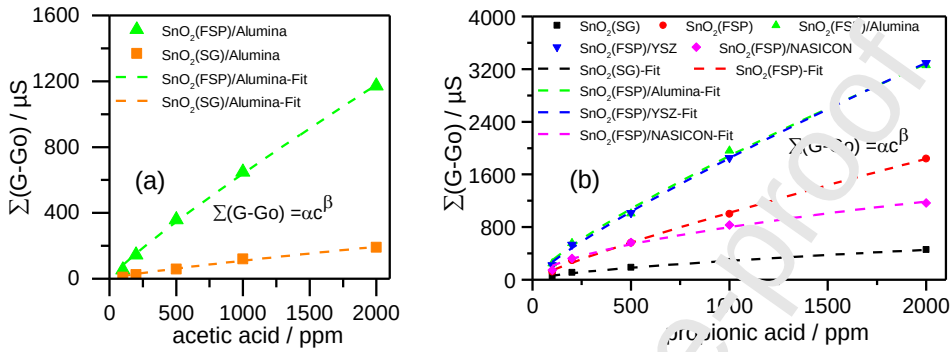

Fig. 17. *Absolute sensor response ∑(G-Go) of a) SnO_2(SG)/Alumina – layer and SnO_2(FSP)/Alumina – layer vs. concentration of acetic acid and b) of several layers vs. concentration of propionic acid.*

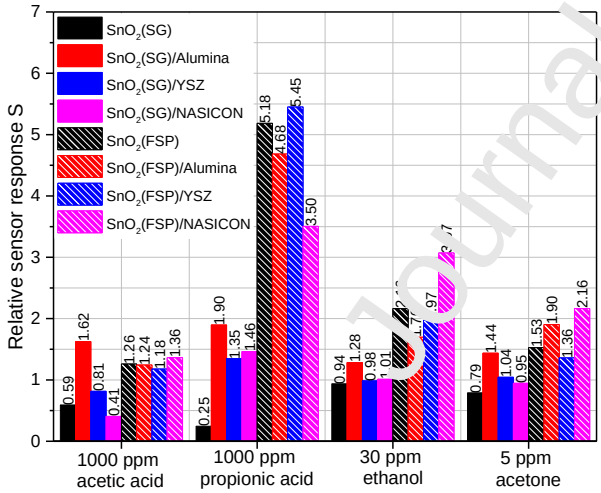

Fig. 18. *Comparison of relative sensor response S (eq. 3) of different SnO_2(SG) and SnO_2(FSP) composites at exposure to different VOCs dissolved in water at pH 3.*

CRedi

Binayak Ojha: Methodology, Investigation, Formal Analysis, Software, Visualization, Data Curation, Writing-Original Draft, Writing-Review & Editing. **Margarita Aleksandrova:** Investigation, Formal Analysis. **Matthias Schwotzer:** Investigation, Formal Analysis. **Matthias Franzreb:** Writing-Review & Editing. **Heinz Kohler:** Conceptualization, Methodology, Writing-Original Draft, Writing-Review & Editing, Supervision, Project Administration, Funding acquisition

Decla

☒The authors declare that they have no known competing financial interests or personal relationships that could have appeared to influence the work reported in this paper.

☐The authors declare the following financial interests/personal relationships which may be considered as potential competing interests: